

PENNSTATE



Applied Research Laboratory

North Atherton Street, PO Box 30, State College, PA 16804
Telephone: (814) 865-8938 Fax: (814) 865-8896 Email: jwl@wt.arl.psu.edu

August 30, 2004

Dr. Kam W. Ng
OFFICE OF NAVAL RESEARCH
BALLSTON CENTRE TOWER ONE
800 NORTH QUINCY STREET
ARLINGTON VA 22217-5660
Subject: *FINAL REPORT: N00014-01-1-0325*

Enclosures: (2) SF298 and final report, *Advancement and Application of Multiphase CFD Modeling to High Speed Supercavitating Flows*, by J.W. Lindau, R.F. Kunz, dated August 20, 2004.

Dear Kam:

Enclosed please find one copy of the final report and associated SF298 for award number, N00014-01-1-0325, *Advancement and Application of Multiphase CFD Modeling to High Speed Supercavitating Flows*.

Sincerely

Jules W. Lindau
Research Associate

cc:

DEFENSE TECHNICAL INFORMATION CENTER
8725 JOHN J KINGMAN ROAD STE 0944
FORT BELVOIR VA 22060-6218

NAVAL RESEARCH LABORATORY
ATTN: CODE 5227
4555 OVERLOOK AVENUE SW
WASHINGTON DC 20375-5320

OFFICE OF NAVAL RESEARCH REGIONAL OFFICE CHICAGO
536 S CLARK STREET ROOM 208
CHICAGO IL 60605-1588

REPORT DOCUMENTATION PAGEForm Approved
OMB No. 0704-0188

Public reporting burden for this collection of information is estimated to average 1 hour per response, including the time for reviewing instructions, searching existing data sources, gathering and maintaining the data needed, and completing and reviewing the collection of information. Send comments regarding this burden estimate or any other aspect of this collection of information, including suggestions for reducing this burden to Washington Headquarters Service, Directorate for Information Operations and Reports, 1215 Jefferson Davis Highway, Suite 1204, Arlington, VA 22202-4302, and to the Office of Management and Budget, Paperwork Reduction Project (0704-0188) Washington, DC 20503.

PLEASE DO NOT RETURN YOUR FORM TO THE ABOVE ADDRESS.

1. REPORT DATE (DD-MM-YYYY) 8/20/04		2. REPORT DATE 8/20/04		3. DATES COVERED (From - To) 1 January 2001-30 December 2003	
4. TITLE AND SUBTITLE Advancement and Application of Multiphase CFD Modeling to High Speed Supercavitating Flows				5a. CONTRACT NUMBER N00014-01-1-0325	
				5b. GRANT NUMBER N00014-01-1-0325	
				5c. PROGRAM ELEMENT NUMBER	
				5d. PROJECT NUMBER	
6. AUTHOR(S) Jules W. Lindau Robert F. Kunz				5e. TASK NUMBER	
				5f. WORK UNIT NUMBER	
7. PERFORMING ORGANIZATION NAME(S) AND ADDRESS(ES) The Pennsylvania State University Applied Research Lab P.O. Box 30 State College, PA 16804-0030				8. PERFORMING ORGANIZATION REPORT NUMBER	
9. SPONSORING/MONITORING AGENCY NAME(S) AND ADDRESS(ES) OFFICE OF NAVAL RESEARCH Ballston Centre Tower One 800 North Quincy Street Arlington, VA 22217-5660				10. SPONSOR/MONITOR'S ACRONYM(S) ONR	
				11. SPONSORING/MONITORING AGENCY REPORT NUMBER	
12. DISTRIBUTION AVAILABILITY STATEMENT UNLIMITED					
13. SUPPLEMENTARY NOTES					
<div style="text-align: right; font-size: 2em; font-weight: bold;">20040920 058</div>					
14. ABSTRACT Recent progress in the development and application of homogenous multiphase CFD methods for large-scale gas cavities in liquid flows are presented. The focus of the presentation is on work in n-species transport approaches applied to developed and super-cavitation. Numerical formulation, physical modeling, and applications are included. Numerical issues to be discussed include: preconditioning in the context of incompressible through supersonic Mach numbers, arbitrary numbers of species, high density ratios, and large gas volume/mass fractions; computational grid requirements; dual-time formulation; and general large-scale high-performance computing. Physical modeling issues to be discussed include: homogeneous mixture compressibility; mass-transfer modeling; condensable and non-condensable gas species; turbulence modeling; and 6-degree-of-freedom [6DOF] flowfield/rigid-body interaction. The applications to be presented range from naturally cavitating modeled flow on simple configurations (ogives, nozzles, airfoils/wedges) to more industrially relevant, complex-geometry applications including turbomachinery (cavitation breakdown), and super-cavitation (underwater rockets, hypervelocity darts, condensable and non-condensable cavities, gas-on/off transients, twin-vortex regime). Recent applications including Detached Eddy Simulation [DES] of natural cavities, and 6DOF analysis of a propelled notional super-cavitating vehicle are presented.					
15. SUBJECT TERMS					
16. SECURITY CLASSIFICATION OF:			17. LIMITATION OF ABSTRACT	18. NUMBER OF PAGES 32	19a. NAME OF RESPONSIBLE PERSON Jules W. Lindau
a. REPORT	b. ABSTRACT	c. THIS PAGE			19b. TELEPHONE NUMBER (include area code) 814-865-8938

FINAL REPORT N00014-01-1-0325: Advancement and Application of Multiphase CFD Modeling to High Speed Supercavitating Flows

Jules W. Lindau Robert F. Kunz

APPLICATIONS AND PAYOFF

This research focuses on the application of multiphase CFD modeling for high-speed underwater flows. The payoff for this and other related investigations will be analysis input for High Speed Supercavitating Vehicle (HSSV) designs including test-bed and variable cavitator designs. The tools developed will be used for assessment of candidate cavitator, fin and full-vehicle configurations. They will also provide assessments of experiment vs. prototype correspondence issues such as integrated passive and active controllability, water tunnel blockage, and scaling. Eventually the tools will be evolved to where they can reliably provide predictions of the *in situ* performance capabilities of a given final design, assessment of the limitations of a given design for countermeasure development and ultimately analysis of maneuvering vehicles.

TECHNICAL OBJECTIVES

The overall technical objective of this program has been to develop robust, validated CFD tools for supercavitating flow modeling and apply the analysis capability to HSSV-relevant configurations.

ABSTRACT

Recent progress in the development and application of homogenous multiphase CFD methods for large-scale gas cavities in liquid flows are presented. The focus of the presentation is on work in n-species transport approaches applied to developed and super-cavitation. Numerical formulation, physical modeling, and applications are included. Numerical issues to be discussed include: preconditioning in the context of incompressible through supersonic Mach numbers, arbitrary numbers of species, high density ratios, and large gas volume/mass fractions; computational grid requirements; dual-time formulation; and general large-scale high-performance computing. Physical modeling issues to be discussed include: homogeneous mixture compressibility; mass-transfer modeling; condensable and non-condensable gas species; turbulence modeling; and 6-degree-of-freedom [6DOF] flowfield/rigid-body interaction. The applications to be presented range from naturally cavitating modeled flow on simple configurations (ogives, nozzles, airfoils/wedges) to more industrially relevant, complex-geometry applications including turbomachinery (cavitation breakdown), and super-cavitation (underwater rockets, hypervelocity darts, condensable and non-condensable cavities, gas-on/off transients, twin-vortex regime). Recent applications including Detached Eddy Simulation [DES] of natural cavities, and 6DOF analysis of a propelled notional super-cavitating vehicle are presented.

1 INTRODUCTION

Multiphase flows have received growing research attention among CFD practitioners due in large measure to the evolving maturity of single-phase algorithms that have been adapted to the increased complexity of multicomponent systems. However, there remain a number of numerical and physical modeling challenges that arise in multi-phase CFD analysis beyond those present in single-phase methods. Principal among these are large constituent density ratios, the presence of discrete interfaces, significant mass transfer rates, non-equilibrium interfacial dynamics, compressibility effects associated with the very low mixture sound speeds which can arise, the presence of multiple constituents (viz. more than two) and void wave propagation. These naturally deserve special attention when a numerical method is constructed or adapted for multi-phase flows.

The ability to properly model multiphase flows has significant potential engineering benefit. In particular, liquid-gas flows where a persistent gas phase occupies a significant, large-scale, volume are considered. Large-scale vaporous cavities may appear in flows about submerged objects due to reduction in local static pressure below the local vapor pressure. Such flows represent traditional cavitation. In addition, ventilated, gaseous cavities are present in specialized high speed applications where enhanced cavities are used to improve hydrodynamic performance. A third type of cavitating flow occurs when liquid and gas temperatures are elevated significantly due to stagnation conditions, chemistry, or other heat sources. In this case the equilibrium vapor pressure may be affected by the local temperature. Traditionally, cavitation has had negative implications associated with damage, reduction in hydrodynamic performance, and/ or noise. However, for certain applications, a natural or ventilated supercavity has demonstrated potential benefit. Intentionally-placed supercavities have long been applied in the design of hydrofoils as well as high performance marine propellers. An application of particular interest to the authors is that of a very high speed aquatic vehicle mostly enshrouded in a supercavity, and, thus, experiencing a significantly reduced drag relative to a fully-wetted, counterpart.

Underwater multiphase flows typically involve the presence of compressibility effects in a flow that is largely incompressible. For typical marine applications this is due to the well-known dramatic decrease of the acoustic speed, from either isolated phase, for a homogeneous, liquid-gas mixture [1]. The situation is illustrated in Fig. 1 for a saturated water mixture at 300K. The homogeneous mixture relation for isothermal sound speed has been plotted as a function of vapor volume fraction. Note that, for moderate vapor volume fractions, the sonic velocity is less than 5m/s, which is almost two orders of magnitude less than the sonic velocities in either of the pure phases. As has been noted in many other sources, in the presence of cavitation, velocities normally associated with subsonic, incompressible flows may result in supersonic conditions and associated strong wave formations such as shocks. It is therefore evident that such compressible phenomena must be represented accurately in multiphase simulations.

The class of multiphase flows under consideration here is developed and supercavitating flows, wherein significant regions of the flow are occupied by gas phase, thus the terminology, "large-scale." Depending on the configuration, such "developed" [2] cavities are composed of a mixture vapor and non-condensable gases. Historically, most efforts to model large cavities relied on potential flow methods applied to the liquid flow, while the bubble shape and closure conditions were specified. Adaptations of potential flow methods remain in widespread use today [3], due to their inherent computational efficiency, and their proven effectiveness in predicting numerous first order dynamics of super-cavitating configurations. Recently, more general CFD approaches have been developed to analyze these flows. In one class of methods, a single continuity equation is

considered with the density varying abruptly between vapor and liquid densities through an equation of state. Such “single-continuity-equation-homogeneous” methods have become fairly widely used for sheet and super-cavitation analysis ([4-8], for example). Although these methods can directly model viscous effects, they are inherently unable to distinguish between condensable vapor and noncondensable gas, a requirement of ventilated super-cavitating vehicle analysis. By solving separate continuity equations for liquid and gas phase fields, one can account for and model the separate dynamics and thermodynamics of the liquid, condensable vapor, and noncondensable gas fields. Such multispecies methods are also termed homogeneous because interfacial dynamics are neglected, that is, there is assumed to be no-slip between constituents residing in the same control volume. A number of researchers have adopted this level of differential modeling, mostly for the analysis of natural cavitation where two phases/constituents are accounted for ([9-11], for example). This is the level of modeling employed here, though a multiple species formulation is used to account for N-gaseous fields. For two phases/constituents these methods are very closely related to the “single-continuity-equation-homogeneous” methods addressed above with interfacial mass transfer modeling supplanting an equation of state.

Full-two-fluid modeling, wherein separate momentum (and in principle energy) equations are employed for the liquid and vapor constituents, have also been used to model natural cavitation [12]. However, in sheet-cavity flows, the gas-liquid interface is known to be nearly in dynamic equilibrium; for this reason, we do not pursue a full two-fluid level of modeling.

Developed cavitating flows are characterized by large density ratios (liquid to vapor density ratios of greater than 10^4 is typical of marine cavitation), relatively discrete cavity-free stream interfaces and, due to ventilation, multiple gas phase constituents. Accordingly, the CFD method employed must accommodate these physics effectively. Most relevant applications exhibit large scale unsteadiness associated with re-entrant jets, periodic ejection of non-condensable gas, cavity “pulsations”, and large scale vortices. In addition, we are interested in capturing the flow about maneuvering vehicles with articulated control surfaces. Accordingly, we and others ([7, 10, 11, 13]) employ a time-accurate formulation in the analysis of large scale cavitation.

In the presentation that follows, the governing multiphase physical system will be defined. A local preconditioning methodology, essential to rendering model solutions efficiently and accurately, will be reviewed. The modification to turbulence transport modeling known as Detached Eddy Simulation (DES), as applied to multiphase model solutions presented here, will be described. The method of coupling rigid body motion to multiphase fluid flow as applied to model solutions will also be described. The methods of numerical integration of the governing equations will be given, and finally, a section of computational results is presented. Results supporting the validity and documented the capabilities of the modeling method have been chosen.

NOMENCLATURE	
C_1, C_2	turbulence model constants
C_q	dimensionless ventilation rate $[q/(U_0 D c^2)]$ (q is volume flow rate)
$C_{\text{prod}}, C_{\text{dest}}$	mass transfer model parameter
C_p	specific heat and pressure coefficient
c, c'	sound speed, pseudo-sound speed
D_c	cavitation diameter
Fr	Froude Number $[U_0/(Lg)^{1/2}]$
e	volumetric internal energy
h, h_0	specific enthalpy, specific stagnation enthalpy

k, ε	turbulence model eddy viscosity and dissipation rate
L_t	turbulent length scale
$\dot{m}^+, \dot{m}^-, \dot{\omega}$	mass transfer source terms
P	turbulence model production term
Pr	Prandtl Number
$\sigma_k, \sigma_\varepsilon$	turbulence model Schmidt Numbers for k and ε
p, q, r	vehicle relative rotation rates (also p is thermodynamic pressure)
p_v	saturation vapor pressure
T	temperature
S	rigid-body motion dependent variable vector
t_∞	time parameter in mass transfer model
u_i, U_∞	Cartesian velocity, freestream velocity
x_i	Cartesian coordinate
Y, Y^*	mass fraction, relative (to total gas) mass fraction
y^+	dimensionless wall distance (boundary layer)
$\alpha_l, \alpha_g, \alpha_v$	liquid, gas, and vapor volume fractions
Γ^p	preconditioning matrix
γ_g	specific gravity of vehicle
δ_{ij}	Kronecker delta
$\mu_m, \mu_{m,t}$	mixture molecular, and eddy viscosity
$\kappa_{m,t}$	mixture, turbulent conductivity
$\rho, \tilde{\rho}_l, \tilde{\rho}_g, \tilde{\rho}_v$	mixture, and isolated liquid, gas, and vapor densities
σ	cavitation index $[(p_\infty - p_v)/(0.5\rho_l U_\infty^2)]$

2 MODEL FORMULATION

The physical model is locally homogenous, multifield and single-fluid. Thus the model consists of species conservation equations coupled to a single momentum and energy equations. The form is further refined by a time-dependent (unsteady), Reynolds-Averaged Navier-Stokes (URANS) model using a two-equation turbulence closure. For some applications turbulence modeling is modified via a DES technique [14]. Mass transfer modeling between liquid and vapor phases is achieved with an ad-hoc model described in this section. Although no results including gas-gas mass transfer are presented. Gas phase chemistry modeling, based on the work of Venkateswaran and others [15], follows methodology similar to the liquid-vapor model presented here. Methods of averaging the mixture scalar quantities are based on mass for intensive quantities and volume for all others. Quantities of interest are specific heat, molecular and eddy viscosity, laminar and turbulent Prandtl number, and conductivity.

The differential form of the computational model in Cartesian tensor notation is given in Eqn. 1. The corresponding conservative variables, primitive variables, flux vectors, and source terms are defined in Eqn. 2. This equation differs in appearance from the basic physical system due to

appearance of the term, $\Gamma^p \frac{\partial Q}{\partial \tau}$, a result of the Choi-Merkle, dual-time preconditioned approach [15]. Definition of the preconditioning matrix is given in Subsection 2.1, a description of the DES method, as applied here, is given in Subsection 2.2, and a description of the 6-degree-of-freedom coupled fluid-rigid-body-motion methodology is given in Subsection 2.3.

$$\frac{\partial Q_c}{\partial t} + \Gamma^p \frac{\partial Q}{\partial \tau} + F_{j,j} - F_{j,j}^v = H \quad (1)$$

$$Q = \begin{bmatrix} p \\ u_j \\ T \\ \alpha_g \\ Y_k^* \end{bmatrix} \quad Q_c = \begin{bmatrix} \alpha_l \tilde{\rho}_l \\ \rho u_j \\ e \\ \tilde{\rho}_g \alpha_g Y_v^* \\ \tilde{\rho}_g \alpha_g Y_k^* \end{bmatrix} \quad F_j = \begin{bmatrix} \alpha_l \tilde{\rho}_l u_j \\ \rho u_i u_j + p \delta_{ij} \\ u_j (e + p) \\ \tilde{\rho}_g \alpha_g Y_v^* u_j \\ \tilde{\rho}_g \alpha_g Y_k^* u_j \end{bmatrix} \quad F_j^v = \begin{bmatrix} 0 \\ t_{ij} \\ u_i t_{ij} + \kappa_{m,i} \frac{\partial T}{\partial x_j} \\ 0 \\ 0 \end{bmatrix} \quad H = \begin{bmatrix} \dot{m}^+ + \dot{m}^- \\ 0_i \\ 0 \\ -(\dot{m}^+ + \dot{m}^-) \\ \dot{\omega}_k \end{bmatrix} \quad (2)$$

In the vector form of Eqn. 2, the first equation represents continuity of the liquid-phase written in terms of volume fraction. The next two equations are momentum and energy equations for the *mixture*. The last two equations deserve further comment. They represent individual gaseous species continuity equations. The subscript g is used to denote all gaseous (including vapor) species, while the subscript v denotes the isolated vapor phase and k denotes non-condensable gaseous species. For generality, $k=1, \dots, N$, where N represents the number of non-condensable gaseous species. The tilde above the density indicates that the quantity is defined by the rule of Amagat rather than Dalton, i.e. considering the isolated constituent, rather than the mixture. Note that, the mass fraction and the volume fraction are related: $\rho Y_g = \alpha_g \tilde{\rho}_g$. Further, the mixture density is given by Eqn. 3.

$$\rho = \alpha_g \tilde{\rho}_g + \alpha_l \tilde{\rho}_l = (1 - \alpha_l) \tilde{\rho}_g + \alpha_l \tilde{\rho}_l = \alpha_v \tilde{\rho}_v + \sum_{k=1}^N \alpha_k \tilde{\rho}_k + \alpha_l \tilde{\rho}_l \quad (3)$$

The superscript, *, indicates a *relative* gas mass fraction, defined in Eqn. 4:

$$Y_k^* = \frac{Y_k}{Y_g} = \frac{Y_k}{Y_v + \sum_{k=1}^N Y_k} \quad \text{and} \quad Y_v^* = \frac{Y_v}{Y_g} = \frac{Y_v}{Y_v + \sum_{k=1}^N Y_k} \quad (4)$$

The viscous stress tensor takes on the usual form.

$$t_{ij} = \mu_{m,i} \left(u_{i,j} + u_{j,i} - \delta_{ij} \frac{2}{3} u_{k,k} \right) \quad (5)$$

In Eqn. 6, necessary mixture quantities are defined. The subscript m indicates a liquid-gas mixture quantity. The mixture viscosity and Prandtl number are computed based on a local volume average. The mixture specific heat, is computed based on a mass average.

$$\begin{aligned}
\mu_l &= \frac{\rho C_\mu k^2}{\varepsilon} & \mu_m &= \alpha_l \mu_l + \alpha_v \mu_v + \alpha_k \mu_k & \mu_{m,t} &= \mu_m + \mu_t \\
Pr_m &= \alpha_l Pr_l + \alpha_v Pr_v + \alpha_k Pr_k & C_{p_m} &= Y_l C_{p_l} + Y_v C_{p_v} + Y_k C_{p_k} \\
\kappa_{m,t} &= \left(\frac{\mu_m}{Pr_m} + \frac{\mu_t}{Pr_t} \right) C_{p_m}
\end{aligned} \tag{6}$$

Finally, two-equation turbulence closure is employed.

$$\begin{aligned}
\frac{\partial(\rho k)}{\partial t} + \frac{\partial(\rho k u_j)}{\partial x_j} &= \frac{\partial}{\partial x_j} \left(\left(\mu_m + \frac{\mu_t}{\sigma_k} \right) \frac{\partial k}{\partial x_j} \right) + P - \rho \varepsilon \\
\frac{\partial(\rho \varepsilon)}{\partial t} + \frac{\partial(\rho \varepsilon u_j)}{\partial x_j} &= \frac{\partial}{\partial x_j} \left(\left(\mu_m + \frac{\mu_t}{\sigma_\varepsilon} \right) \frac{\partial \varepsilon}{\partial x_j} \right) + [C_1 P - C_2 \rho \varepsilon] \left(\frac{\varepsilon}{k} \right)
\end{aligned} \tag{7}$$

The transfer of mass between liquid and vapor states is handled with simple finite-rate relations given in Eqn. 8. The mass transfer rate between gaseous species due to chemical reactions is indicated in Eqn. 1 by $\dot{\omega}_k$.

$$\begin{aligned}
\dot{m}^- &= \frac{C_{dest} \tilde{\rho}_l \alpha_l MIN[0, p - p_v]}{\frac{1}{2} \tilde{\rho}_l U_\infty^2 t_\infty} \\
\dot{m}^+ &= \frac{C_{prod} \tilde{\rho}_v (\alpha_l + \alpha_k)^2 \alpha_v}{t_\infty} \\
p_v &= p_v(T)
\end{aligned} \tag{8}$$

The mass-transfer model is presented without rigor. It is supported by its supposed relation to the understood physics: Destruction of liquid is related to the difference of the local pressure, p , and vapor saturation pressure, p_v , and the production of liquid is based on an interpretation of the work of Hohenberg [16]. Further support is afforded by the presented computational results. Within the context of Eqn. 8, saturation vapor pressure is an assumed function of temperature; thermal effects on phase change may be included. C_{dest} and C_{prod} are empirical constants. Unless otherwise noted, for all results presented, $C_{dest}=C_{prod}=100$, and the time scale parameter, t_∞ , is based on a convective time scale roughly related to cavity formation. For modeled cases, where a cavitator is well defined, this time scale has been based on the cavitator diameter and the free stream velocity. For turbomachinery and hydrofoil model problems, this was based on the maximum chord length and the relative inflow velocity. As has been presented in Ref. [17], model results are relatively insensitive to these choices.

In the presented work all walls are adiabatic. The model system is closed with the inclusion of equations of state for the constituent phases and species. For the liquid phase, for instance, $\tilde{\rho}_l = \tilde{\rho}_l(p, T)$ and $h_l = h_l(p, T)$. For the constituent gaseous species, including the vapor, the species density and enthalpy may be expressed similarly. Typically an ideal gas equation of state is employed.

2.1 Local Preconditioning

In order to obtain convergent and accurate numerical solution of a linear algebraic system, the condition number of that system must be sufficiently small. An appropriate definition of the condition number is the magnitude of the ratio of the largest magnitude eigenvalue to the smallest magnitude eigenvalue of the matrix system [18]. The optimal value, therefore, is one. Using the current finite-volume method of discretization, the global algebraic system may be divided into local subsystems considering the solution of equations related to individual control volumes. In order to obtain a well-conditioned system of equations for solution of multiphase, turbulent, viscous, compressible flow problems of interest, it is beneficial to examine and, by rescaling the time-derivative terms, manipulate the inviscid eigensystem. The condition of this subsystem tends to indicate the condition status of the more complex full numerical system. This has been explained in detail in Ref. [15] and is the procedure followed here. The one-dimensional form of the governing multi-phase equations is considered. Extension to multiple dimensions is straightforward and does not effect the conclusions drawn here.

$$\frac{\partial Q_c}{\partial \tau} + \frac{\partial E}{\partial x} = 0 \quad (9)$$

A set of primitive variables may be chosen with the appropriate transformation Jacobian. Here the transformation is not exact but is a preconditioning matrix containing pseudo-properties substituted for the physically correct definitions. These substitutions will be shown to favorably affect accuracy and convergence of the solution method without altering the correct physics of the solution. This form of the equations is given in Eqn. 10. In Eqn. 11, the conservative variables, the fluxes, and two primitive variable sets are defined. One is denoted by the subscript 2 and is convenient for development of the preconditioning matrix. The other is indicated by subscript 1 and is preferred (by the authors) for computations. The elements of these sets are chosen for algebraic convenience in developing the preconditioning matrix.

$$\Gamma_2^p \frac{\partial Q_2}{\partial \tau} + \frac{\partial E}{\partial x} = 0 \quad (10)$$

$$Q_c = \begin{bmatrix} \rho Y_l \\ \rho u \\ e \\ \rho Y_v \\ \rho Y_k \end{bmatrix} \quad E = \begin{bmatrix} \rho Y_l u \\ \rho u^2 + p \\ u(e + p) \\ \rho Y_v u \\ \rho Y_k u \end{bmatrix} \quad Q_2 = \begin{bmatrix} p \\ u \\ T \\ Y_v \\ Y_k \end{bmatrix} \quad Q_1 = \begin{bmatrix} p \\ u \\ T \\ \alpha_g \\ Y_k^* \end{bmatrix} \quad (11)$$

The preconditioning matrix is defined in Eqn. 12. This formulation has been given in Ref. [19]. A similar but more detailed preconditioning derivation for the 2-phase, liquid-vapor system, was given in Ref. [20].

$$\Gamma_2^p = - \begin{bmatrix} Y_i \frac{\partial \rho'}{\partial p}|_2 & 0 & Y_i \frac{\partial \rho}{\partial T}|_2 & -\rho + Y_i \frac{\partial \rho}{\partial Y_v}|_2 & -\rho + Y_i \frac{\partial \rho}{\partial Y_j}|_2 \\ u \frac{\partial \rho'}{\partial p}|_2 & \rho & u \frac{\partial \rho}{\partial T}|_2 & u \frac{\partial \rho}{\partial Y_v}|_2 & u \frac{\partial \rho}{\partial Y_j}|_2 \\ \left(1 - \rho \frac{\partial h}{\partial p}|_2\right) + h_0 \frac{\partial \rho'}{\partial p}|_2 & \rho u & \rho \frac{\partial h}{\partial T}|_2 + h_0 \frac{\partial \rho}{\partial T}|_2 & \rho \frac{\partial h}{\partial Y_v}|_2 + h_0 \frac{\partial \rho}{\partial Y_v}|_2 & \rho \frac{\partial h}{\partial Y_j}|_2 + h_0 \frac{\partial \rho}{\partial Y_j}|_2 \\ Y_v \frac{\partial \rho'}{\partial p}|_2 & 0 & Y_v \frac{\partial \rho}{\partial T}|_2 & \rho + Y_v \frac{\partial \rho}{\partial Y_v}|_2 & Y_v \frac{\partial \rho}{\partial Y_j}|_2 \\ Y_i \frac{\partial \rho'}{\partial p}|_2 & 0 & Y_i \frac{\partial \rho}{\partial T}|_2 & Y_i \frac{\partial \rho}{\partial Y_v}|_2 & \delta_{ij} \rho + Y_i \frac{\partial \rho}{\partial Y_j}|_2 \end{bmatrix} \quad (12)$$

The corresponding flux Jacobian, $A_2 = \frac{\partial E}{\partial Q_2}$, is given in Eqn. 13.

$$A_2 = \begin{bmatrix} u Y_i \frac{\partial \rho}{\partial p}|_2 & \rho Y_i & u Y_i \frac{\partial \rho}{\partial T}|_2 & -\rho u + u Y_i \frac{\partial \rho}{\partial Y_v}|_2 & -\rho u + u Y_i \frac{\partial \rho}{\partial Y_j}|_2 \\ 1 + u^2 \frac{\partial \rho}{\partial p}|_2 & 2\rho u & u^2 \frac{\partial \rho}{\partial T}|_2 & u^2 \frac{\partial \rho}{\partial Y_v}|_2 & u^2 \frac{\partial \rho}{\partial Y_j}|_2 \\ \rho u \frac{\partial h}{\partial p}|_2 + u h_0 \frac{\partial \rho}{\partial p}|_2 & \rho h_0 + u^2 & \rho u \frac{\partial h}{\partial T}|_2 + u h_0 \frac{\partial \rho}{\partial T}|_2 & \rho u \frac{\partial h}{\partial Y_v}|_2 + u h_0 \frac{\partial \rho}{\partial Y_v}|_2 & \rho u \frac{\partial h}{\partial Y_j}|_2 + u h_0 \frac{\partial \rho}{\partial Y_j}|_2 \\ u Y_v \frac{\partial \rho}{\partial p}|_2 & \rho Y_v & u Y_v \frac{\partial \rho}{\partial T}|_2 & \rho u + u Y_v \frac{\partial \rho}{\partial Y_v}|_2 & u Y_v \frac{\partial \rho}{\partial Y_j}|_2 \\ u Y_i \frac{\partial \rho}{\partial p}|_2 & \rho Y_i & u Y_i \frac{\partial \rho}{\partial T}|_2 & u Y_i \frac{\partial \rho}{\partial Y_v}|_2 & \delta_{ij} \rho u + u Y_i \frac{\partial \rho}{\partial Y_j}|_2 \end{bmatrix} \quad (13)$$

In each of these matrices, in the last row and last column, indexing over the number of noncondensable gaseous species is implied. Thus the definition extends to an arbitrary number of species. The eigenvalues of the preconditioned system are given in Eqn. 14.

$$\lambda\left(\left[\Gamma_2^p\right]^{-1} A_2\right) = \left(u, u, \frac{1}{2} \left[u \left(1 + \left(\frac{c'}{c} \right)^2 \right) \pm \sqrt{u^2 \left(1 - \left(\frac{c'}{c} \right)^2 \right)^2 + 4c'^2} \right] \right) \quad (14)$$

The *preconditioned*, pseudo-sound speed, c' , is given in Eqn. 15. In Eqn. 14, c is the physical sound speed. Note that, c , the isentropic, frozen mixture sound speed is given by removing the primes from Eqn. 15.

$$c'^2 = \frac{\rho \frac{\partial h}{\partial T}|_2}{\rho \frac{\partial \rho'}{\partial p}|_2 \frac{\partial h}{\partial T}|_2 + \frac{\partial \rho}{\partial T}|_2 \left(1 - \rho \frac{\partial h}{\partial p}|_2\right)} \quad (15)$$

An appropriate preconditioner definition for the pseudo-sound speed is the magnitude of the local convective velocity. The appropriateness of this definition may be confirmed by applying Eqn. 14. The resulting eigensystem is well-conditioned for all Mach numbers independent of important effects such as phasic density ratio and sound speed. As is the case with low-Mach number preconditioning for single-phase flows, in numerical practice, the pseudo-sound speed value should be lower limited [15]. For applications presented here, this lower limit was chosen based on the free stream velocity magnitude. For cases where the free-stream phase is modeled as incompressible, the optimal lower limit was found to be the square-root of ten times the free stream magnitude. For all other cases, the lower limit was set equal to that magnitude. Other more rigorous methods of limiting the local preconditioning definition have been derived in Ref. [21]. These definitions have been applied with success to the physical system outlined here. However, no results based on this methodology are presented. Another requirement is that the preconditioned system should revert to the physically exact system when the local velocity magnitude is supersonic. In this case the physical system is automatically well conditioned. Therefore, in computational practice, the physical sound speed is substituted for the pseudo-sound when the local Mach number is greater than one. This should yield a continuous transition from preconditioned to physical system at the sonic point. Further discussion of the appropriate choice of pseudo-properties is given in Ref. [15].

The computational form chosen is given by primitive variable set 1. Therefore, transformation is necessary. The transformation is obtained using the Jacobian relating variable set 1 to set 2 as shown in Eqns. 16 and 17.

$$\Gamma_1^p \frac{\partial Q_1}{\partial \tau} + \frac{\partial E}{\partial x} = 0 \quad (16)$$

$$\Gamma_1^p = \frac{\partial Q_2}{\partial Q_1} \Gamma_2^p \quad (17)$$

The transformation Jacobian is given by Eqn. 18.

$$\frac{\partial Q_2}{\partial Q_1} = \begin{bmatrix} 1 & 0 & 0 & 0 & 0 \\ 0 & 1 & 0 & 0 & 0 \\ 0 & 0 & 1 & 0 & 0 \\ \frac{\partial Y_v}{\partial p}|_1 & 0 & \frac{\partial Y_v}{\partial T}|_1 & \frac{\partial Y_v}{\partial \alpha_g}|_1 & \frac{\partial Y_v}{\partial Y_j^*}|_1 \\ \frac{\partial Y_i}{\partial p}|_1 & 0 & \frac{\partial Y_i}{\partial T}|_1 & \frac{\partial Y_i}{\partial \alpha_g}|_1 & \frac{\partial Y_i}{\partial Y_j^*}|_1 \end{bmatrix} \quad (18)$$

2.2 Detached Eddy Simulation

Detached Eddy Simulation (DES) and other hybrid RANS-Large Eddy Simulation (LES) approaches have emerged recently as a potential compromise between RANS based turbulence models and full LES. Specifically, for flows characterized by large scale separation and unsteadiness, DES has been shown by a number of workers to date to provide improved mean flow predictions [14, 22, 23].

DES is a generalization of RANS modeling. The underlying turbulence model for DES is a RANS subgrid model with the characteristic length scale reinterpreted in terms of the local grid scale. When the local mesh is fine relative to the turbulence mixing length, the DES model becomes an LES with a Smagorinsky-like subgrid closure [14]. In these resolved regions, modeling error is minimized. The solution remains RANS elsewhere and retains the solution efficiencies of RANS.

DES is formulated for and is particularly suited to regions of massive separation where RANS closures are challenged. With minimal increases in grid density, the governing equations are allowed to support the most energetic turbulence scales yielding improved solution fidelity. Near boundaries, where kinematic constraints limit the scale of turbulence eddies and where grid resolution demands for traditional LES are most demanding, DES reverts back to RANS. By design, RANS models can perform very well near solid surfaces.

In the context of the k - ϵ model given in Eqn. 7, a DES variant is obtained by defining a modified turbulence energy destruction term as (see [14] for example):

$$-\rho\epsilon \rightarrow -\rho\epsilon \cdot F_{DES} \quad (19)$$

$$F_{DES} \equiv \text{MAX} \left[\frac{L_t}{C_{DES}\Delta}, 1 \right], L_t \equiv \frac{k^{3/2}}{\epsilon}, \Delta \equiv \text{MAX}(\delta_x, \delta_y, \delta_z)$$

2.3 Fluid-Rigid-Body Coupled Motion

The multiphase fluid dynamics model is coupled to the general equations of vehicle/rigid body motion (6DOF). Thus the unsteady flow (URANS) and the 6DOF are submodels to be coupled for solution of the overall model problem. Coupling between the submodels is achieved via modeling the shear and normal forces on the surface of the rigid body. The shear and normal forces are results of the instantaneous solution to the URANS. In this model, the normal forces include both the pressure on solid surfaces and the impulse through propulsion and ventilation computational boundaries. Shear forces are computed based on a turbulent wall function. The URANS forces are then resolved into appropriate instantaneous force and moment components for the 6DOF. The result of the 6DOF solution is then translation and rotation of the rigid body. With adequate discretization, the 6DOF and the URANS then tend to the proper physics. The current presentation and results are for a single, completely rigid, body and closely follow the methodology of Dreyer [24] for single-phase flow. Formulation of the single-phase pseudocompressible formulation for nonstationary grid systems has been well presented by Taylor [25]. Solutions with multiple bodies, or a single body with articulated control surfaces, represent straightforward extensions of the current methodology.

Computation of fully coupled multiphase URANS-6DOF modeling is achieved with a computational flow grid fixed to the rigid body. Flow solution is then obtained in an inertial reference frame. The rigid body motion problem is solved in a body-fixed reference frame. These choices follow the work of Dreyer et al. [24]. During each physical time step, the hydrodynamic

forces on the body are computed based on the instantaneous flow field solution, then the position of the body, is updated based upon solution of the 6DOF equations, and then the flow solution is updated. More detail related to this method is given in Ref. [26].

2.4 Numerical Integration

The described model flow and rigid body motion equations are solved in the UNCLE-M code. The flow solver is structured, multiblock, implicit and parallel with upwind flux-difference splitting for the spatial discretization and Gauss-Seidel relaxation for the inversion of the implicit operator. Primitive variable (MUSCL) interpolation with limiting based on the solution volume fraction is applied to retain higher order accuracy in flow fields containing physical discontinuities. Source term linearization is approached on a case-by-case basis. However, it has been found that for flows with free-stream phase Mach numbers approaching the incompressible limit, in keeping with previous work [27], those source terms associated with vapor production should be linearized for inclusion in the implicit linear system left-hand-side. Terms associated with liquid production are treated explicitly and under-relaxed with a factor of 0.1. For cases with compressible free-stream Mach numbers, it has been found that, depending on initial conditions, full source-term linearization is appropriate. With typical initial conditions, until the residual drops one to two orders of magnitude, under-relaxation with no source-term linearization, combined with reduced integration step size, may be the best approach. After this start-up effort, full-linearization with larger integration steps usually is effective. This procedure is in accordance with the work of Venkateswaran et al. [15]. At each pseudo-time step, the turbulence transport equations are solved subsequent to solution of the mean flow equations. Further details regarding the numerical method are available in Ref. [27]. For cases with rigid body motion, the 6DOF model is a set of six ordinary differential equations in time and is integrated with a five-stage, fourth-order Runge-Kutta method. The same integration method was used by Dreyer et al. [24].

3 APPLICATIONS

Several multiphase, compressible and incompressible, two and three-phase flowfields have been modeled. These flows include validating cases compared to experimental results, as well as demonstrative cases highlighting physically sensible results and capabilities of the modeling method.

3.1 Cavitating Flow in a Venturi

Reboud, Stutz, et al. [28] have performed detailed unsteady, flowfield measurements of vaporous cavitating flow in the two-dimensional Venturi section of a water tunnel. The test section captures significant physics found on the suction side in a blade passage. Thus their experiment and the current model results represent partially cavitating flow in a turbomachinery-like environment. In Fig. 2, the average and RMS fluctuating portions of the liquid volume fraction is presented based on the modeled flow. This figure serves to illustrate the geometry of the modeled test section as well as the results obtained during modeling. The test section had a height at the throat equal to 43.7 mm and a constant width equal to 44 mm. The nominal cavity length for comparison here was 80 mm in the horizontal direction. The nominal angle of the lower surface of the Venturi downstream of the throat, with respect to a horizontal line, was 4° . The experiments were conducted at Reynolds numbers based on cavity length from 4.3×10^5 to 2.1×10^6 and at a range of cavitation numbers, based on the upstream pressure and velocity, from 0.6 to 0.75. It may be seen from the figure that although there is a high degree of unsteadiness in the region of the cavitating

flow, this unsteadiness is confined to the test section area. This is consistent with the commentary [28].

In Fig. 3, the current computational results are presented with the experimental data [28]. In the figure, results have been plotted at the five measurement stations used in the experiments. Each of these stations is given at a horizontal position. The experimental cavity was initiated due to the suction peak on the lower surface of the throat of the test section, a reference position of $x=0$. In part (a) of the figure, the mean vapor volume fraction is plotted at the five axial stations. Clearly the model tends to over estimate the void fraction, particularly at the forward region of the cavity, at $x=22.5\text{mm}$. However, the average quantities are in excellent agreement at the tail end. Similar agreement is demonstrated with the unsteady portion of the RMS void fraction, part (b). Here, the error is greater in the closure region, at $x=60\text{mm}$ and $x=80\text{mm}$. Considering the difficulty of modeling in the closure region, this level of agreement is also pleasing. In part (c), the average axial velocity is given, and, in part (d), the RMS fluctuating component is given at the five measurement stations. Here the agreement is generally good, except at the tail end for the average velocity, where the reverse flow is missed. It should be noted that, by application of a two-phase Navier-Stokes model based on a barotropic state law, Reboud et al. [28] were able to obtain similarly good agreement with the experimental data.

3.2 Naturally Cavitating Flow over Axisymmetric Bodies

Turbulent, naturally cavitating flow over axisymmetric bodies is known to be a highly nonlinear and three-dimensional event. This is clearly illustrated in Fig. 4. Here, a photograph during water tunnel testing of a blunt cavitator at zero angle-of-attack, $\sigma \approx 0.35$, and $Re_D \approx 1.5 \times 10^5$ is shown in part (a) to be compared and contrasted to the model result in part (b). To obtain the model result, turbulent vaporous cavitating flow over a blunt cavitator was modeled. σ was set to 0.4 and Re_D was 1.46×10^5 . An appropriate high Reynolds number grid with approximately 1.2 million nodes was used. The snapshot of part (b) represents a physical time slice taken after a clear model cavity cycle had been established. In the figure, an isosurface at $\alpha = 0.5$ has been presented with selected streamlines, and the surface of the cylinder has been colored by volume fraction. The streamlines are merely suggestive (but helpful), as they have been generated based on instantaneous velocity vectors. Clearly in neither the model result nor the photograph is the flowfield in and around the cavity axisymmetric. It is suspected that physical, chaotic, dynamic interdependencies are responsible. Via an adequate level of modeling, a characteristic of the real flow has been well captured. Positive understanding of the causal mechanisms is a subject for further research.

Dependence of the nature of the result on the method of numerical integration has been determined to be minimal. This was done by numerical experiment. The object of this experiment was to determine if the helical reentrant jet procession was dependent on the current method of integration, even though the computational grid was axially symmetric. A portion of the result is shown in Fig. 4c. Possible bias was hypothesized to come from such factors as initial Gauss-Seidel sweep direction, etc. The entire model state from the unsteady integration results for a steadily clockwise processing jet was transformed to a mirror image of that state. This physical mirror state was then used as initial conditions to complete the experiment. All other parameters were unaltered, including the structured grid numbering and computational (i,j,k) coordinates. Integration results on both the mirror and the original solutions were then compared. The solutions were found to be mirror images of each other. Solutions had statistically identical but opposite helical, reentrant flows; one processed clockwise and the other in the counterclockwise direction. All other quantitative comparisons showed identical but mirror-image solutions.

3.3 Propeller Cavitation Breakdown Analysis

A no-skew unducted propeller, designated P4381, was tested by Boswell [30] as part of a larger effort to parameterize ahead powering, blade-rate, fluctuating loads, cavitation inception, cavitation thrust breakdown, structural integrity, and backing performance with consideration of the effect of blade skew. The cavitation thrust breakdown performance of the propeller was determined in a water tunnel at a Reynolds number (based on relative incident velocity and chord at 70% of the span) ranging from 1.38 to 2.44×10^6 . Measurements were taken at specific advance ratios while incrementally dropping the tunnel operating pressure. This process reduced the test cavitation index in a prescribed fashion. Thus, sufficient data were obtained to complete a map of thrust and torque over a range of advance ratios and cavitation indices.

For the UNCLE-M model cases, the Reynolds number based on free stream velocity and diameter was held constant at 1.63×10^6 . For the advance ratios modeled, this is equivalent to a range of Reynolds numbers based on relative incident velocity and chord at 70% span from 1.37 to 2.51×10^6 . This range corresponds to advance ratios ranging from 0.6 to 1.0 . The design advance ratio was given by Boswell [30] to be $J=0.889$. At advance ratios less than approximately 0.6 and greater than 1.0 , the UNCLE-M integrations of the steady form of the equations on the computational grid used here failed to converge. Results presented here were integrated based on solution of the steady-state equations; i.e., physical time derivatives were set to zero. It is suspected that the lack of convergence to the steady-state equations is due to the large scale of unsteadiness inherent in multiphase and high angle-of-attack flows. When such inherent unsteadiness becomes too large to resolve with steady-state physics, it is typical that UNCLE-M will fail to converge to a steady state result but will converge with application of the time dependent formulation [17]. In addition to requiring unsteady integration, it is suspected that proper resolution of the large scale structure of such unsteadiness would necessitate additional and/or better placement of grid points. The grid used was designed with a topology conforming to low incidence flow without attempting the fine resolution of structures like leading edge separation eddies and tip vortices. These structures were only captured in some average sense and when the minimum pressure in such features became important, the overall results suffered. Such features are generally not significant for breakdown prediction at and around the design advance ratio.

The computational grid used with UNCLE-M to obtain breakdown results contained approximately 1.2 million grid points, distributed on 34 processors. A portion of the grid on the propeller surface is shown in Fig. 5. Although the computation was carried out over a single blade passage, taking advantage of azimuthal periodicity, here the grid has been replicated five times to give the appearance of a complete rotor. Results at design advance ratio and three significant cavitation indices are also shown in Fig. 5. This picture shows modeled flow with no significant cavitation, at $\sigma = 1.5$, with significant cavitation in breakdown, at $\sigma = 1.0$, and with significant cavitation and in severe thrust breakdown, at $\sigma = 0.6$. Note that at this low incidence angle, it appears that cavitation is initiated downstream of the leading edge, near the suction peak.

Results are summarized in Fig. 6. As seen in the plots, Boswell compiled the torque and thrust for the P4381 at a wide range of advance ratios and cavitation numbers. It should be noted that, during UNCLE-M computations, surface shear forces were found to add approximately 5 to 10% of the computed torque and remove 1 to 4% from the computed thrust. These fractions were higher at more lightly loaded conditions. Integrated thrust and torque presented here include the shear forces. In addition to plotting the variation in integrated thrust and torque relative to significant parameters, at selected advance ratios and cavitation numbers, Boswell included pictures and diagrams depicting the extent of cavitation over the propeller. Similar presentation of UNCLE-M results is

given in Fig. 7 (a), for flow at a high blade loading condition. Fig. 7 (b) includes a drawing and photograph from the original report by Boswell. Here the cavity extent predicted by UNCLE-M is seen to roughly coincide with the sketch due to Boswell, only on the outer span of the blade. The exact cavity shape is somewhat different. Here, and at a higher angles of attack, leading edge separation plays a larger role in cavity initiation than at the design incidence calculations shown in Fig. 5. Note the cavity extension into the tip vortex region. Although the grid used here is inadequate to resolve tip vortex induced cavitation, it is clear that the predicted, attached cavity persists in the initial region of the (poorly resolved) vortex.

In Fig. 6 the torque and thrust breakdown behavior versus advance ratio is plotted over a range of cavitation indices. UNCLE-M results are represented with open symbols and data from the experiments conducted by Boswell are represented with faired curves. Due to the typical operating conditions of a vehicle, of primary interest is the behavior near the design point and at reduced values of advance ratio. It is supposed that in the hypothetical case of an advance ratio greater than design, the situation would correspond to windmilling or an attempt to slow down or reverse. These represent transient events, not properly addressed here. Therefore, attention is called to the distribution of results produced by UNCLE-M over the range of advance ratios equal to 0.9 and below. For this range, agreement of numerical prediction with experimental data is considered good. At every condition where a converged solution was obtained, torque predictions appear to agree within 5% of the experimental results. The agreement with actual values of thrust is not quite as good as in the case of torque. However, for more highly loaded cases, the agreement between computations and experiment is still good.

It should be noted that the actual prediction of breakdown would be based on the prediction of a critical advance coefficient. This location is sometimes based on some fractional reduction in torque or thrust from the nominal design value. Typically this reduction is 2-5% of the nominal value. It appears that the results from UNCLE-M, based on either integrated thrust or torque, were sufficiently accurate to make this prediction. With proper application of a Reynolds-Averaged Navier-Stokes solver, a high level of agreement should be attainable. The excellent agreement shown over most of the cases for both thrust and torque indicates that high fidelity predictions can be made, and with further refinement, reduction of the error in the thrust prediction at those few points where error was significant should be attainable.

3.4 Multiphase, High Speed Flow

Two applications of interest are considered that involve the modeling of two-phase compressibility effects. Fig. 8 shows an underwater supersonic projectile. Both computational results and a corresponding photograph [31] of an actual test are included in the figure. The three-dimensional, but axisymmetric, computational grid is comprised of 48,049 (in the plane displayed) grid points, and second-order spatial accuracy is used. The flow Mach number for the case shown is 1.03 and the liquid to vapor density ratio is nominally 1000. The experiments and the computations show the presence of a bow shock upstream of the nose. In addition, because of the high velocity, the cavitation number is about 10^{-4} . Consequently, with the exception of the nose which is in compression, the flow immediately adjacent to the body is completely vaporized as is the downstream wake portion.

The second example shown in Fig. 9, is the plume flowfield of an underwater rocket exhaust. The plume exhaust is supersonic and is slightly underexpanded. It is surrounded by a coflowing secondary subsonic gas stream, which in turn is surrounded by a liquid water free-stream flow. The nominal liquid to gas density ratio is 1000. The two-dimensional computational grid is comprised

of 33,153 grid points and second-order spatial accuracy is used. Fig. 9 shows the shock function field, which exhibits the classic expansion pattern. In particular, the interaction of the compressible gas stream with the incompressible liquid is demonstrated first by the contraction and then by the expansion of the gas stream. In addition, the interface between the liquid and gas phases is comprised of a two-phase mixture, which is also fully supersonic due to the low magnitude of the mixture sound speed.

3.5 The Transition from Reentrant to Twin-Vortex Cavity Closure

Of primary concern, is the nature of cavity closure behind a supercavitating object. The mode of cavity closure has a significant impact on cavity and hence stability. A frequently encountered mode of closure behind large cavities is the reentrant jet. This phenomenon has been long studied and described in detail by Franc [32]. Another form of cavity closure occurs, usually downstream of controlled ventilated cavities. This is the twin-vortex type of cavity closure [2]. For a typical cavitator, depending on the Froude Number, the mode of cavity closure (either reentrant or twin vortex) may be plotted as shown in Fig. 10. Here results for a ventilated cavity, behind a conical cavitator, obtained by Stinebring [2], are shown. In this figure as the ventilation rate increases, the cavity pressure increases (σ decreases), and, to a certain extent, the cavity size increases as well. Significantly, as the ventilation flow rate is increased, a transition point is found and the closure transitions from a reentrant jet to a twin-vortex mode. This transition occurs as a hysteresis phenomenon. Thus, there is a region of cavity pressure separating the two flow regimes that appears to be physically unreachable. In Fig. 11, a photograph of a cavity in reentrant closure mode is shown next to computational results at a dimensionless volumetric ventilation flow rate ($C_q = q/U_\infty D_c^2$) of 0.13. The reentrant mode of closure is highlighted by both the overall cavity shape as well as the streamlines shown in the computational result. In Fig. 12, a photograph of the twin-vortex closure mode behind the cavitator is shown next to the computational result at a dimensionless volumetric ventilation rate of 0.51. Clearly, as seen in the photograph, the twin vortex closure flow is much more stable than the reentrant flow of Fig. 11. The computed twin vortex flow, shown in Fig. 12, is also highlighted by streamlines, and the cavity shape clearly shows the twin vortices. All of these results are at $Fr=9$, the same as plotted in Fig. 10. Clearly, the computational results exhibit the correct mode of closure.

3.6 Naturally Cavitating Flow with DES

Fig. 13 shows the schematic of a hydrofoil as offered in [33]. The nominally two-dimensional configuration is mounted at a 7° angle-of-attack and run at two different cavitation indices as well as single phase. Though DES can only simulate the largest scales of turbulence when applied three-dimensionally, in order to provide experience and guidance with the model, "2D DES" runs were performed for the same two cases. All of the simulations (except single phase) were carried out in a time accurate fashion. Specifically, for all of the 2D simulations, a timestep of $\Delta t^* = \Delta t/(c/U_\infty) = 0.0005$ was specified, based on a series of URANS studies performed on the $\sigma=0.8$ case. A formal Δt study was not performed, since as seen below, even after 60,000 timesteps, the simulations are not fully stationary. Still, this value resolves each dominant re-entrant ejection event with on the order of 10,000 timesteps. For the 2D simulations, 10 pseudo-timesteps are run for each physical timestep, as justified in [17].

The inflow velocity was set to a constant value of 6m/s. An inlet turbulence intensity of 0.01 and turbulence length scale of $.0005*$ the channel height were specified. The liquid and vapor densities were set to 1000 and 1 kg/m³ respectively. The constant liquid and vapor sound speeds were set to

1500 and 420 m/s respectively. The cavitation number was defined in terms of the average value of p_R (see Fig. 13), by accumulating the average of this time-varying quantity as the simulations proceeded.

3.6.1 2D Results

Five sets of 2D simulations were performed. A single phase computation was carried out as well as two simulations each at cavitation numbers of 0.4 and 0.8. The single phase calculation converged to a steady state, but the multiphase simulations exhibited highly unsteady behavior. Unsteady RANS analysis was performed for each of $\sigma=0.4, 0.8$. Also, a “2D DES” simulation was performed at each of these cavitation numbers.

Fig. 14, and Table 1, provide details of the 2D results that were obtained. The quantities to computed are time averaged lift and drag coefficients, and various cavity shape parameters. Though lift and drag are unambiguously computed, determination of the average cavity shape can be somewhat discretionary. Specifically, in Fig. 14, the time average cavity shape (defined as the time average contour of $\alpha_L=0.9$) is shown for each of the 2D cases. The cavitation detachment location near the leading edge is easily extracted from this plot. The maximum cavity length, though uniquely defined, is less informative than when simple cavity models are applied, due to the complex shape of the cavity near its trailing edge. Similar ambiguities apply in extracting the maximum cavity thickness. Nevertheless, rather than attempt to smooth or fair the predicted average cavity shape in order to obtain a comparison measure more representative of simpler cavity models, the authors have reported the absolute maxima shown in Fig. 14. The average total vapor volume ($V_v = \sum \alpha_v V_{\text{cell}}$) is provided in Table 1, for the four 2D cases, as an additional indicator of bubble size. (Reported volumes assume a spanwise extent of 0.1m).

Table 1 provides a summary of the predicted lift and drag coefficients and various cavity size parameters (length/diameter, maximum length, maximum thickness, initiation length to maximum thickness, all divided by chord, and vapor volume) for the 2D runs.

Time average quantity	Single Phase	$\sigma=0.8$		$\sigma=0.4$	
		2D	“2D DES”	2D	“2D DES”
C_L	0.624	0.492	0.501	0.198	0.171
C_D	0.024	0.080	0.097	0.068	0.069
L_d/c	NA	.0045	.0050	.0077	.0084
L_{max}/c	NA	1.03	1.09	1.28	1.36
t_{max}/c	NA	0.17	0.22	0.17	0.19
$L_{t_{\text{max}}}/c$	NA	0.66	0.91	0.73	0.80
$V_v (10^{-3} \text{m}^3)$	NA	2.74	4.38	5.66	7.53

TABLE 1. PREDICTED CAVITATION PARAMETERS

3.6.2 3D Results

For the 3D DES simulations, the timestep was doubled to $\Delta t^*=0.0010$ and the number of inner iterates halved to five. Only the $\sigma=0.8$ case has been completed. A large timestep URANS run was first performed to initialize the simulation. This was followed by a 30,000 timestep DES run with one pseudo-timestep per physical timestep. The “final” DES run reported here was run for 30,000 timesteps using 5 pseudo-timesteps per physical timestep. This required approximately 20,000

processor hours on a Cray T3E, for a total wall clock turnaround time of about a week on 100 processors.

The resulting flow field prediction exhibits a highly three-dimensional unsteady character as indicated in Fig. 15. There, a composite of $\alpha_L=0.9$ isosurfaces are presented for 21 timesteps between $t^*=15$ and 25^* . Resolved large scale features include spanwise, streamwise and horseshoe vortical structures, a spanwise oscillatory pinching off of the vapor bubble by a re-entrant jet in the leading edge region, merging and splitting of geometrically complex vapor structures, and spanwise wave structures propagating axially along the cavity interface near the leading edge. Fig. 16 shows an instantaneous view of the predicted $\alpha_L=0.9$ isosurface along with a number of particle pathlines colored by static pressure, indicating the complex vortical nature of the DES flow, including significant axial vorticity which vapor structures tend to track.

3.7 Fully Coupled Multiphase Flow to Rigid-Body-Motion

A three-field (liquid, vapor, noncondensable gas) computation of turbulent mixture flow, fully coupled, via 6DOF modeling, to a supercavitating vehicle was executed. This 1.2 million node, 48 processor computation, executed on a Cray T3E system, was facilitated by a generous grant of *Challenge* computing resources from the US Department of Defense High Performance Computing Modernization Program (HPCMP).

The modeled vehicle is shown in Fig. 17. Fig. 17 (a) contains a schematic drawing and the basis for the notional CFD model. Fig. 17 (b) shows a close-up of the cavitator and ventilation port area. This is from a steady-state computation of flow around the vehicle and illustrates the properly resolved behavior of flow around the cavitator region. The flow separates and natural cavitation is initiated at the corner of the flat cavitator. This cavitation is sufficient to envelope the gas deflectors which aid in the direction of recirculatory ventilation gas exhausting from three axisymmetric ports. The ventilation gas thus enhances and stabilizes the cavity. Due to, among several other factors, this recirculatory feature, it is supposed that a very low rate of ventilation flow should be sufficient to support a rather large cavity. Thus it is important that this effect be captured by the flow model.

Snapshots of computed flow field are shown in Fig. 17 (c). Time histories of vehicle position and velocity are shown in Figure 18. For this computation, the Reynolds Number based on the length of the body, Re_L , is 2.3×10^8 , and the Froude Number (based on vehicle length) is 13.2. The saturation vapor pressure, p_v , used in the source term for liquid vapor mass-transfer, Eq 8, is determined based on the cavitation index, σ , which is equal to 0.02. The cavity ventilation rate, C_q is 4.4. The vehicle specific gravity, γ_g is 1.3 with a uniform density. The vehicle inertial properties were estimated by subdividing the geometry into conical and cylindrical sections similar to the description by Dzielski and Kurdila [34].

In Fig. 17 (c), the vehicle is evident within the supercavity, and appears to exhibit a limit cycle behavior. This is supported by the plots in Fig. 18; where time histories of vehicle position, velocity components and rotation rates are shown. A limit cycle is expected for a vehicle with no control surfaces or method of active stabilization. In the snapshots showing the dynamic behavior of the vehicle, the cavity surface is illustrated with an isosurface of liquid volume fraction equal to 0.5, and the surface of the vehicle is colored by pressure. These snapshots (from dimensionless time 1.2 to 1.55) show a cycle encompassing a complete oscillatory period. This is clear when the snapshots are compared with the zoomed-in vehicle ahead velocity plot shown in Fig. 18 (e). Here a peak is shown at 1.2 and again at 1.55. It is at these peaks that the high amplitude restoring force due to impact with the cavity wall occurs. Note the vehicle *skips* off of the lower cavity surface periodically, and the impact with the liquid induces a high pressure on the impact region. This

impact reduces the ahead velocity and drives the vehicle upward slightly. The upward motion, concurrent with the reduction in forward velocity, can be seen in the plot of absolute vertical position. This sequence explains the remarkable inherent stability of the propelled, supercavitating vehicle as configured here and is referred to as planing mode behavior [35].

In Fig. 18 (f), dynamic characterization of the long term behavior of the 6DOF UNCLE-M model of the supercavitating vehicle is illustrated. The phase plot of vehicle relative vertical velocity, and ahead velocity, is shown versus time. Although a simple periodic behavior is not expected from a dynamic model that has millions of degrees of freedom, it is evident that, based on the nearly repeating closed loop pattern, a quasi-periodic, developed limit-cycle is in place. This is apparent at around 3.5 time units onward, and is denoted in the figure. It is expected that more refined blowing and propulsion flow rates should result in a condition with much smaller amplitude limit-cycle oscillations. The addition of control surfaces, such as cavity piercing fins, should also reduce oscillations and, possibly, reduce the vertical drift of the vehicle.

4 SUMMARY

A multiphase CFD method has been presented and applied to a number of high density ratio sheet and supercavitating flows. This presentation begins with a description of the multiphase mixture physical model, a locally homogeneous, multispecies, compressible form, including mass transfer modeling, turbulence modeling, and fully coupled flow to rigid body motion. Several aspects of the method were outlined and demonstrated that enable convergent, accurate and efficient simulations of these flows. These include a preconditioned differential model with favorable eigensystem characteristics, regardless of phasic density ratio, a multiple species formulation that separately accounts for condensable and non-condensable gases, higher order flux differencing with limiters, large scale turbulence simulation via DES, and the embedding of this scheme in a parallel multi-block Navier-Stokes platform.

The cases examined, both validative and demonstrative, show the capabilities of the computational method over a range of important flow conditions. Computations suggest that UNCLE-M has the ability to correctly represent the overall nature of unsteady, complex, multiphase flows. This in itself is a validation of the approach taken here. The current approach has allowed rendering of unsteady multiphase flows at Reynolds numbers relevant to engineering applications in a modeling method amenable to complex geometries and design applications.

The authors continue to develop the capabilities of UNCLE-M. This includes the pursuit relevant validation cases for complex, unsteady, turbulent, high-speed, multiphase flows. It would seem that with the current level of physical modeling, combined chemistry and phase change high-speed flows should be tractable. These capabilities, in addition to the already demonstrated abilities to model buoyancy, ventilation, propulsion, and fully coupled multiphase-fluid to rigid-body-motion, are critical to a current research goal, the full configuration, design-quality modeling of a controlled, high speed supercavitating vehicle undergoing maneuvers.

5 REFERENCES

- [1] Brennen, C.E., 1995, *Cavitation and Bubble Dynamics*, Oxford University Press, New York.
- [2] Stinebring, D.R., Billet, M.L., Lindau, J.W., Kunz, R.F. Developed cavitation-cavity dynamics, *VKI Special Course on Supercavitating Flows*, February 2001.
- [3] Kirchner, I. N. Numerical modeling of supercavitating flows, *VKI Special Course on Supercavitating Flows*, February 2001.

- [4] Dellanoy, Y., Kueny, J.L., Two-phase flow approach in unsteady cavitation modeling, *ASME FED-Vol. 98*, pp.153-158 1990.
- [5] Dieval, L., Pellone, C., Arnaud, M. Advantages and disadvantages of different techniques of modeling of supercavitation, *Proceedings of Meeting on High Speed Hydrodynamics and Supercavitation*, Grenoble, France 2000.
- [6] Reboud, J. L., Delannoy, Y. Two-phase flow modeling of unsteady cavitation, *Proceedings of 2nd International Symposium on Cavitation*, Tokyo, Japan, 1994 pp. 39-44.
- [7] Song, C., He, J., Numerical simulation of cavitating flows by single-phase flow approach, *Proceedings of 3rd International Symposium on Cavitation*, Grenoble, France, 1998, pp. 295-300.
- [8] Van der Heul, D.R., Vuik, C., Wesseling, P. Efficient computation of flow with cavitation by compressible pressure correction, *Proceedings of AMIF-ESF Workshop on Computing Methods for Two-Phase Flow*, Aussois, France 2000.
- [9] Ahuja, V., Hosangadi, A., and S. Arunajatesan, Simulations of cavitating flows using hybrid unstructured meshes, *ASME Journal of Fluids Engineering*, Vol. 123, No. 2, 2001.
- [10] Merkle, C.L., Feng, J., Buelow, P.E.O. Computational modeling of the dynamics of sheet cavitation, *Proceedings of 3rd International Symposium on Cavitation*, Grenoble, France, 1998, pp. 307-311.
- [11] Shin, B.R., Ikohagi, T. A numerical study of unsteady cavitating flows, *Proceedings of 3rd International Symposium on Cavitation*, Grenoble, France, 1998, pp. 301-306.
- [12] Grogger, H.A., Alajbegovic, A., Calculation of the cavitating flow in venturi geometries using two fluid model, *ASME Paper FEDSM 98-5295*, 1998.
- [13] Reboud, J. L., Fortes-Patella, R., Hofman, M., Lohrberg, H., Ludwig, G., Stoffel, B. Numerical and experimental investigations on the self-oscillating behaviour of cloud cavitation, *ASME Paper FEDSM99-7259, Proceedings of 3rd ASME/JSME Joint Fluids Engineering Conference*, 1999.
- [14] Strelets, M. Detached eddy simulation of massively separated flows, *AIAA paper 2001-0879, 39th Aerospace Sciences Meeting and Exhibit*, Reno, Nevada, 2001.
- [15] Venkateswaran, S. and Merkle, C. L., Analysis of preconditioning methods for the Euler and Navier-Stokes equations, *Von Karman Institute Lecture Series*, 1999-03, March, 1999.
- [16]. Hohenberg, P.C. and B.I. Halperin, Theory of dynamic critical phenomena, *Reviews of Modern Physics*, 49(3), pp. 435-479, 1977.
- [17]. Lindau, J.W., Kunz, R.F., Boger, D.A., Stinebring, D.R., and H.J. Gibeling, High Reynolds number, unsteady, multiphase CFD modeling of cavitating flows, *Journal of Fluids Engineering, Transactions of ASME*, vol. 124(3) pp. 607-616, 2002.
- [18]. Golub, G.H. and C.F. van Loan, *Matrix Computations*, 3rd Ed., The Johns Hopkins University Press, Baltimore, MD, 1996.
- [19]. Lindau, J.W., Venkateswaran, S., Kunz, R.F. and C.L. Merkle, Computation of compressible multiphase flows, *AIAA 2003-1285*.

- [20]. Lindau, J.W., Venkateswaran, S., Kunz, R.F. and C.L. Merkle, Development of a fully-compressible multiphase Reynolds-averaged Navier-Stokes model, AIAA 2001-2648.
- [21]. Venkateswaran, S. Li, D. and C. L. Merkle, Influence of stagnation regions on preconditioned solutions at low speeds, AIAA 2003-0435.
- [22]. Mitchell, A., Morton, S., and Forsythe, J., Analysis of delta wing vortical substructures using detached-eddy simulation, AIAA 2002-2968, *40th Aerospace Sciences Meeting and Exhibit*, Reno, Nevada, 2002.
- [23]. Hedges, L.S., Travin, A.K., and Spalart, P.R. Detached-eddy simulations over a simplified landing gear, *Journal of Fluids Engineering*, Vol. 124, pp. 413-423, 2002.
- [24]. Dreyer, J., Taylor, L., Zierke, W., and F. Davoudzadeh, A first-principle approach to the numerical prediction of the maneuvering characteristics of submerged bodies, *ASME Fluids Engineering Division Summer Meeting* 1997.
- [25]. Taylor, L.K. *Unsteady Three-Dimensional Incompressible Algorithm Based on Artificial Compressibility*, Doctoral Dissertation, Mississippi State University, 1991.
- [26]. Lindau, J.W., Kunz, R.F., Mulherin, J.M., Dreyer, J.J., and D.R. Stinebring, Fully coupled, 6-DOF to URANS, modeling of cavitating flows around a supercavitating vehicle, *Fifth International Symposium on Cavitation (CAV2003)*, Osaka, Japan, November 1-4, 2003.
- [27]. Kunz, R.F., Boger, D.A., Stinebring, D.R., Chyczewski, T.S., Lindau, J.W., Gibeling, H.J., Venkateswaran, S., and T.R. Govindan, A preconditioned Navier-Stokes method for two-phase flows with application to cavitation predication, *Computers and Fluids*, 29, pp. 849-875, 2000.
- [28]. Reboud, J., Stutz, B. and O. Coutier, Two-phase flow structure of cavitation: experiment and modelling of unsteady effects, *Third International Symposium on Cavitation*, Grenoble, France, 1998.
- [29]. Stinebring, D.R., Billet, M.L., and J.W. Holl, An investigation of cavity cycling for ventilated and natural cavities, *Technical Memorandum, TM 83-13*, The Pennsylvania State University Applied Research Laboratory, 1983.
- [30]. Boswell, R.J., Design, cavitation performance and open-water performance of a series of research skewed propellers, Naval Ship Research and Development Center, Wasington, DC, Report 3339, March 1971.
- [31]. Kirschner, I.N., Results of selected experiments involving supercavitating flows, *RTO AVT/VKI Special Course on Supercavitating Flows*, von Karman Institute for Fluid Dynamics, Rhode Saint Genese, Belgium, 2001.
- [32]. Franc, J.P., Partial cavity instabilities and re-entrant jet, Pasadena, Cav2001, CA, 2001.
- [33]. Franc, J.P., Schnerr, G.H. Workshop on physical models and CFD tools for computation of cavitating flows, call for participation in present workshop, *5th International Symposium on Cavitation*, CAV2003, Osaka, Japan 2003.
- [34]. Dzielski, J. and A. Kurdila, A benchmark control problem for supercavitating vehicles, an initial investigation of solutions, *Journal of Vibration and Control*, 9(7) pp. 791-804, 2003.
- [35]. Kirschner, I.N., Kring, D.C., Stokes, A.W., Fine, N.E., and J.S. Uhlman, Control strategies for supercavitating vehicles, *Journal of Vibration and Control*, 8(2) pp. 219-242, 2002.

6 FIGURES

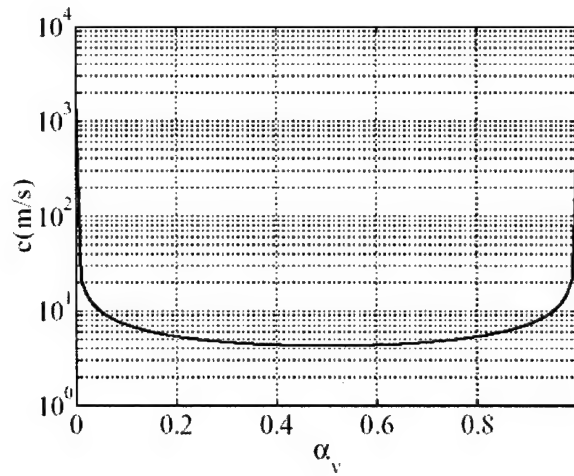


Figure 1: Equilibrium mixture sound speed for water at 300K.

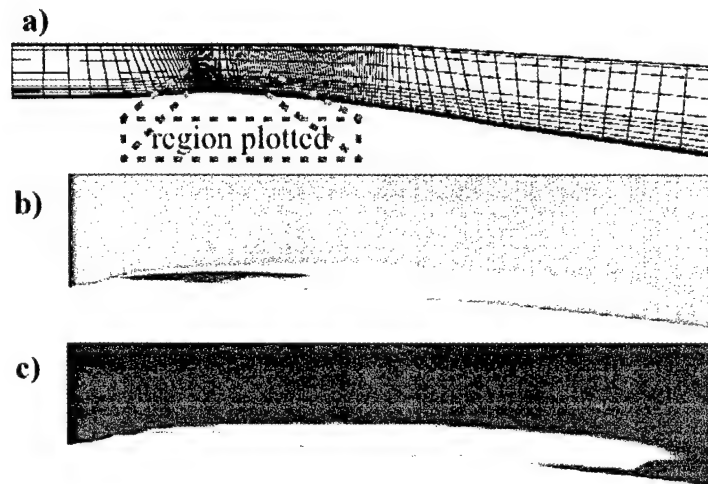


Figure 2: Computational result. Unsteady, naturally cavitating, two-dimensional flow. $Re_L = 7.1 \times 10^5$ (based on cavity length). Modeling of a two-dimensional cavitation tunnel. Ref. [28].

a) Grid with every 4th point shown.

b) Mean liquid volume fraction; red, $\alpha_v > 0.995$; blue, $\alpha_v < 0.005$.

c) RMS fluctuating component of liquid volume fraction; red indicates a value of 0.5 or greater; blue indicates negligible fluctuating component.

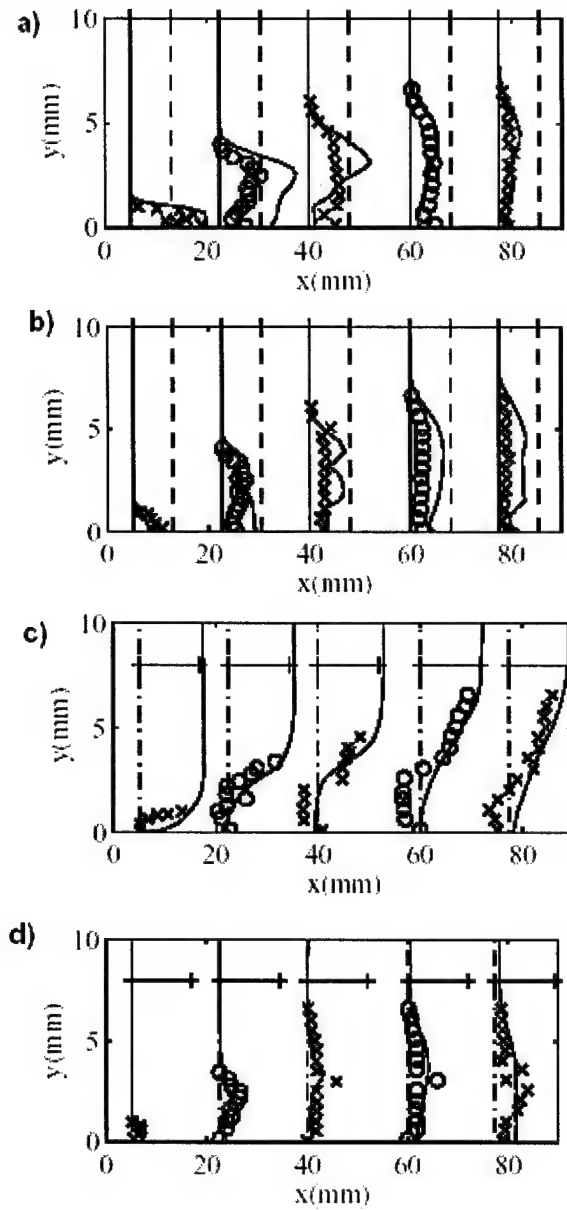


Figure 3: Comparison of modeled, unsteady cavitating flow to measurements at five horizontal stations [28]. y , vertical distance from wall. x , horizontal distance downstream of throat.

a) Mean vapor volume fraction (α_v).

b) Fluctuating RMS vapor volume fraction.

(At each station, solid line indicates 0 and dashed line indicates 0.5.)

c) Mean horizontal velocity.

d) Fluctuating RMS horizontal velocity.

(Horizontal bars at stations indicate 12m/s, the approximate free stream velocity).

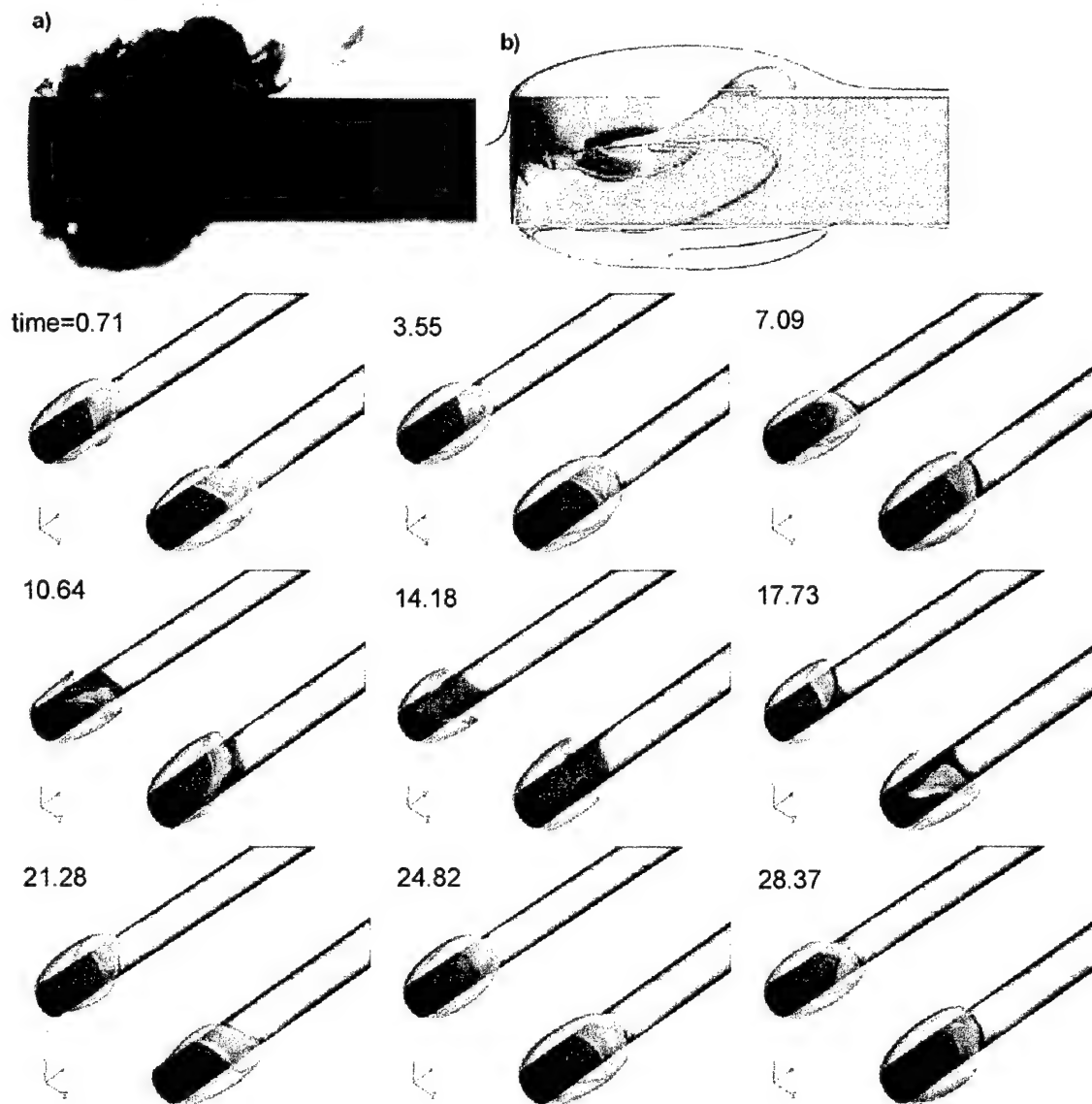
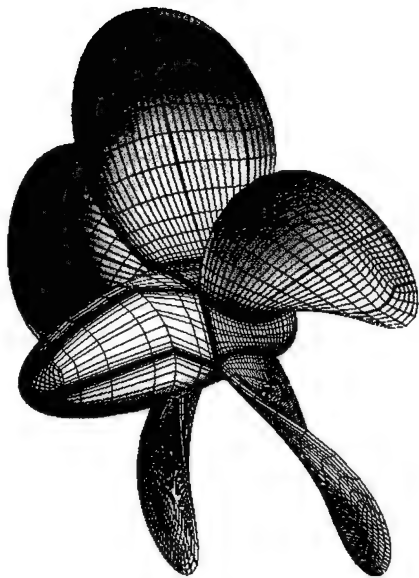


Figure 4: Blunt cavitator at zero angle-of-attack:

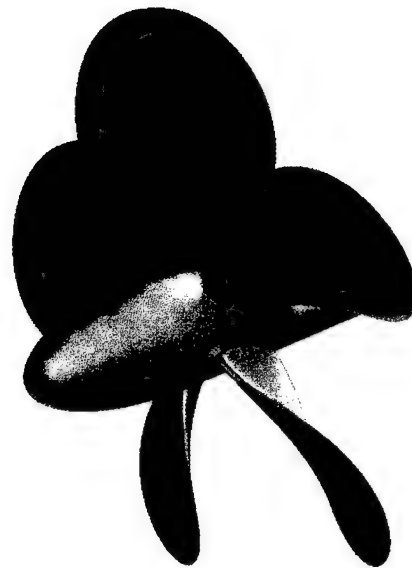
a) In water tunnel at $\sigma=0.35$.

b) Model result from UNCLE-M at $\sigma=0.4$. Isosurface (translucent) at $\alpha_t=0.5$. Selected (instantaneous) streamlines. Surface of cylinder colored by α_t (red, $\alpha_t > 0.995$; blue, $\alpha_t < 0.005$).

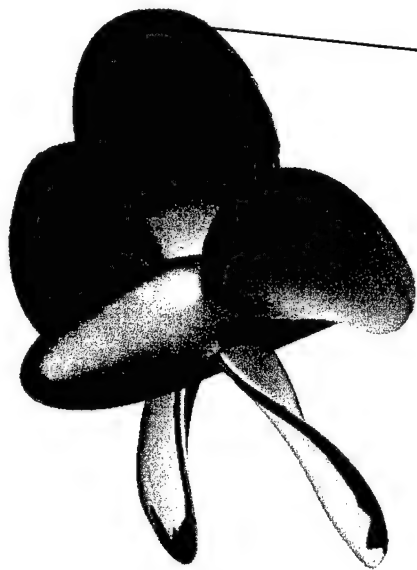
c) Experiment to identify nonphysical biasing. Sequence of two model results at $\sigma=0.35$. The solution in the upper left (reflection) of each snapshot originated from conditions obtained from the time-dependent solution in the lower right. To obtain the upper left solution, this common origin was transposed to a mirror image condition. Isosurface at $\alpha_t=0.5$, cylinder colored by pressure (red, $C_p > 0.25$, blue $C_p < -0.3$). Strouhal time indicated $\left[\frac{tU_\infty}{D} \right]$ from a reference zero (not the complete integration time).



Portion of grid on surface. Every 4th
point from block boundary to block



σ



σ



σ

Figure 5: UNCLE-M results. Grid and flow over P4381 at design advance ratio, $J=0.889$. Results at three cavitation indices with surface colored by pressure and a gray isosurface of liquid volume fraction ($\alpha_f=0.5$).

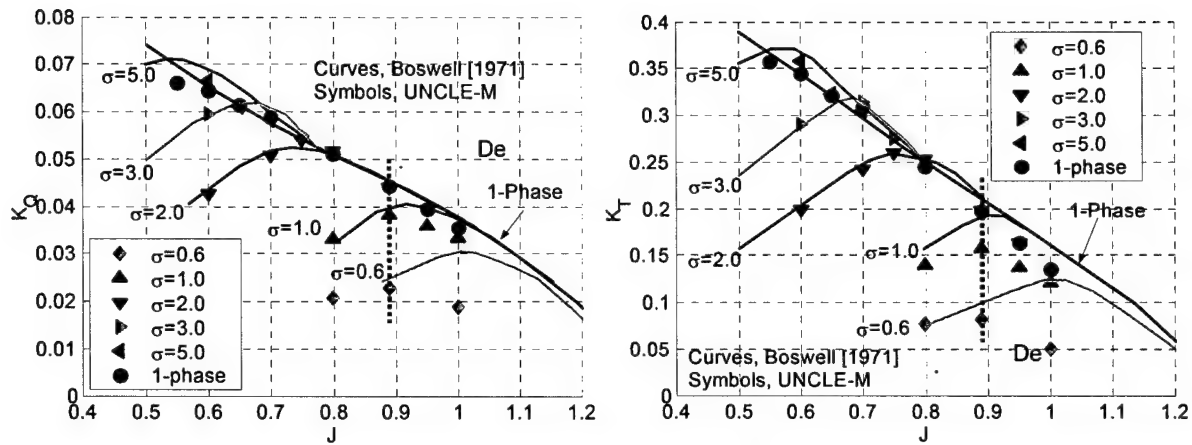


Figure 6: Unducted propeller torque coefficient [$K_Q = (\text{Torque}) / (\rho n^2 D^5)$] and thrust coefficient [$K_T = (\text{Thrust}) / (\rho n^2 D^4)$] versus advance ratio over a range of cavitation indices, experimental data [30] and UNCLE-M results.

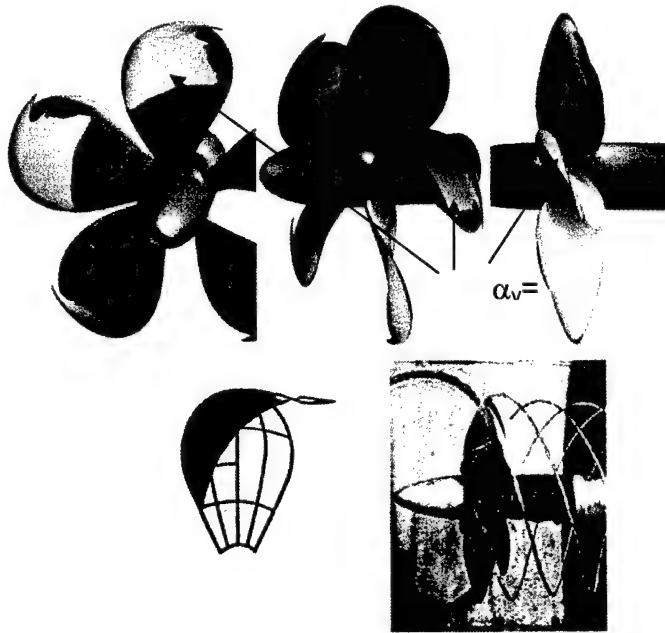


Figure 7: Flow over P4381, $J=0.7$, $\sigma=3.5$.

- UNCLE-M solution, three views showing surface colored by pressure and a gray isosurface of liquid volume fraction.
- Diagram and picture from Boswell [1] indicating extent of experimentally observed cavitation.

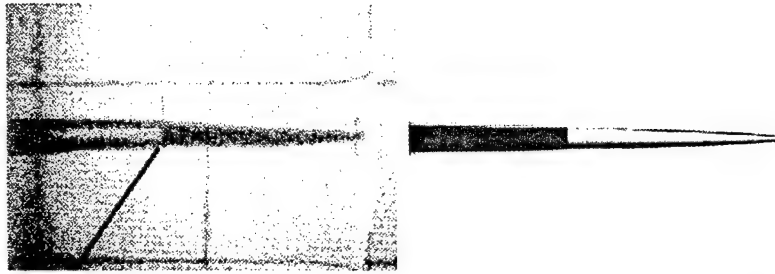


Figure 8: Photograph [31] and model result of supersonic underwater projectile. Model result contains flow field density contours indicating bowshock and vaporous wake.

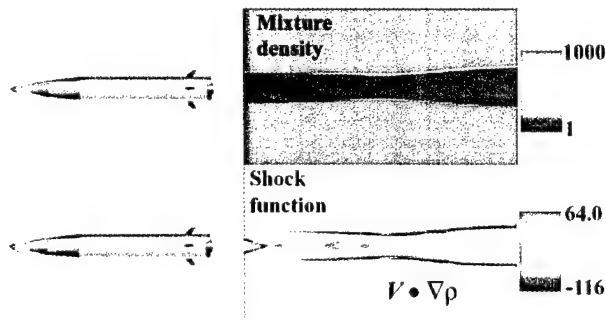


Figure 9: Cartoon vehicle and 3-stream, axisymmetric aft flow region. Supersonic gas (air) center jet (diameter=1), surrounded by subsonic gas (air, at free stream velocity with outer diameter=2), surrounded by subsonic liquid, water.

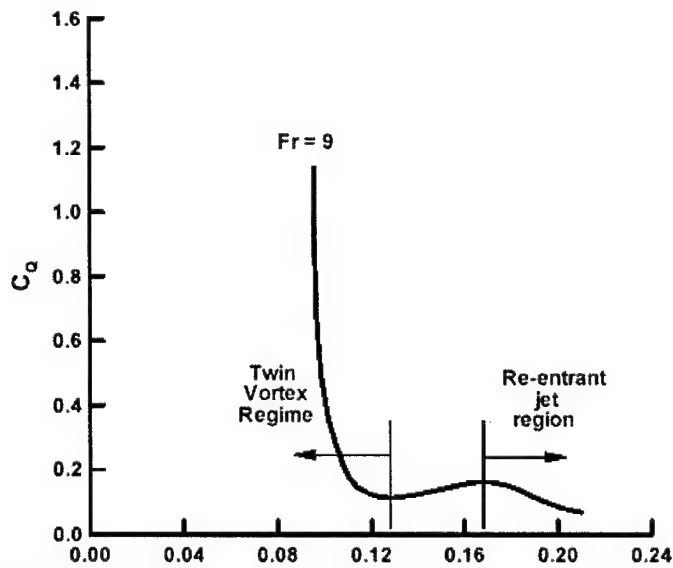


Figure 10: Experimentally observed modes of cavity closure for flow behind a conical (45°) ventilated cavitator.

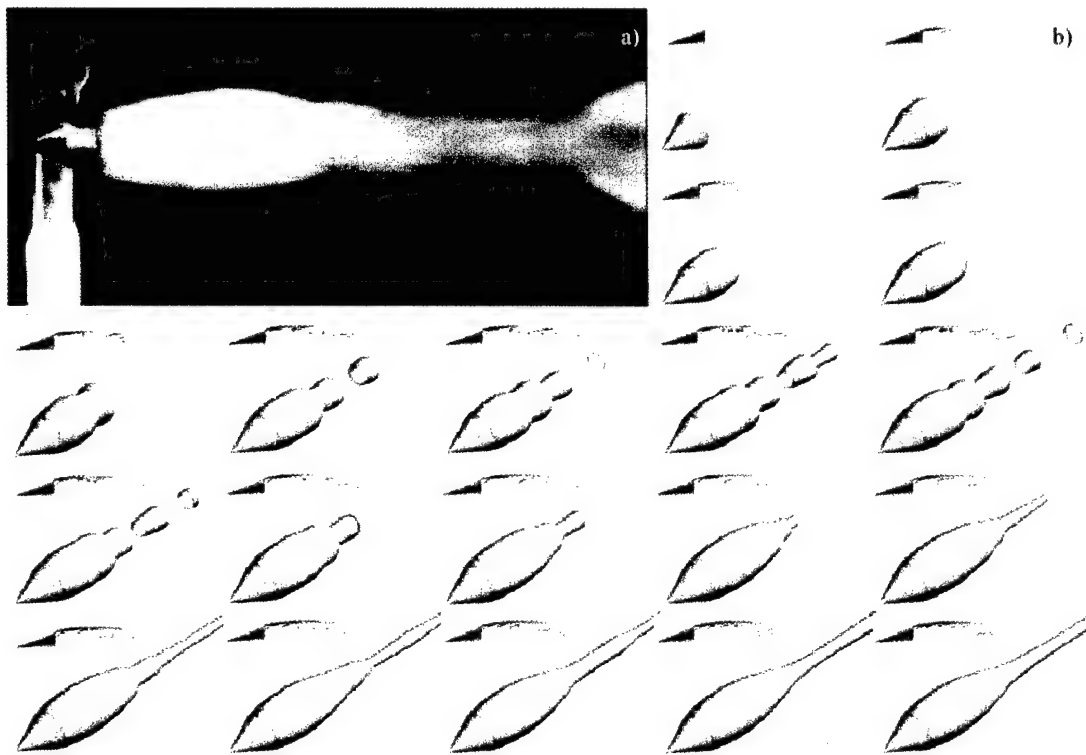


Figure 11: a) Photograph of a ventilating strut mounted 45° conical cavitator in the 12" water tunnel at the Applied Research Laboratory.
 b) Time history of the gas-on-transient presented as snapshots of (blue) isosurfaces of $\alpha_t = 0.95$. Streamlines shown in red.

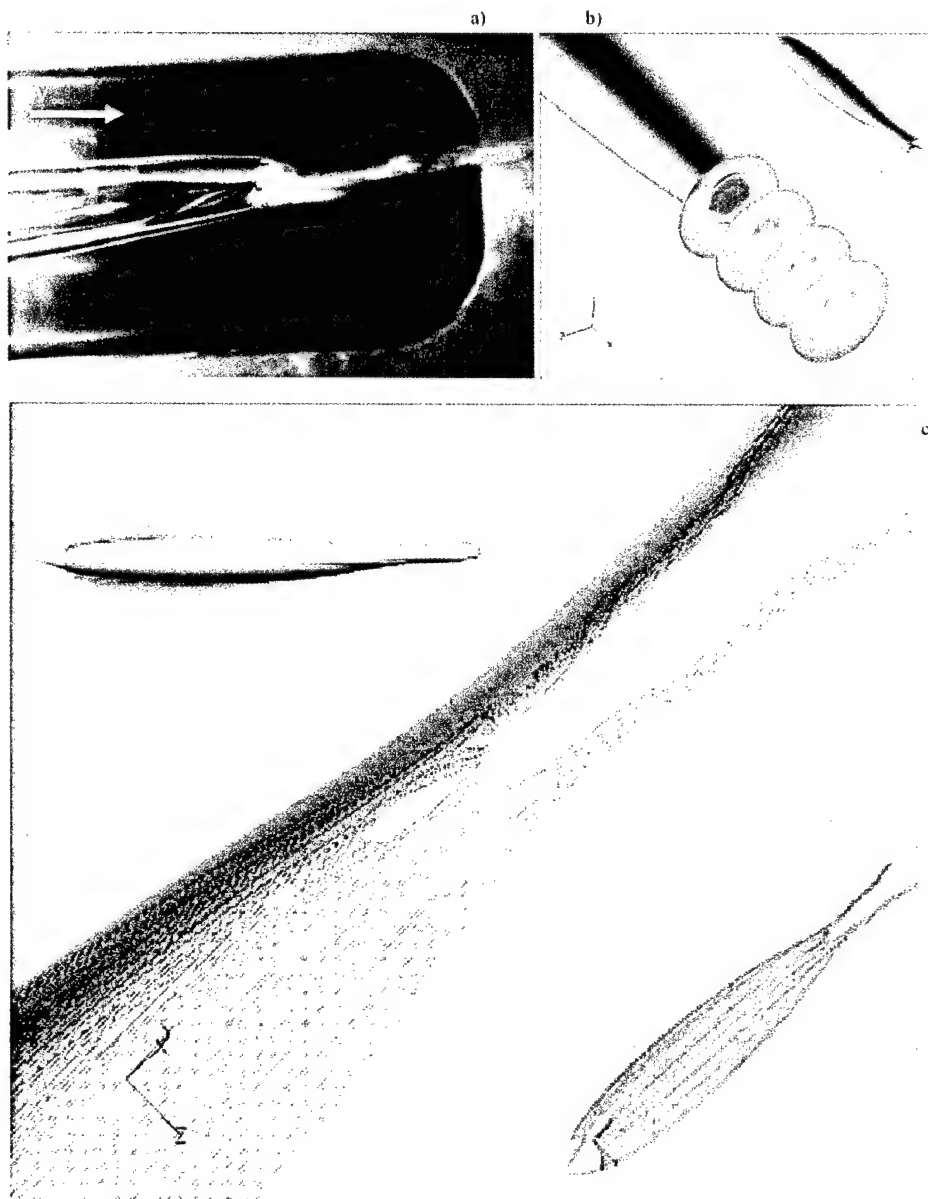


Figure 12: Twin vortex cavity closure

a) Photograph of the aft end of the cavity of a 45° conical cavitator, ventilating in the twin vortex regime, taken in the 12" water tunnel at the Applied Research Laboratory.

b) Predicted isosurface of $\alpha = 0.5$ and selected stagnation pressure contours.

c) Farfield pressure contours and selected cavity streamlines illustrating the twin-vortex nature of the cavity flow.

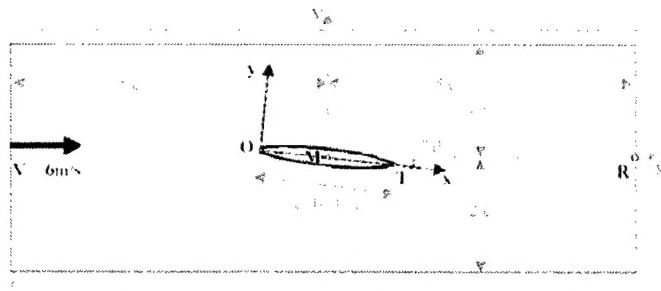


Figure 13: Geometric parameters of hydrofoil configuration.



Figure 14: Predicted time average contours of $\alpha_L = 0.9$ for the four 2D runs performed. These were used to determine reported cavity geometric parameters. Red: $\sigma=0.8$, URANS, Blue: $\sigma=0.8$, "2D DES", Green: $\sigma=0.4$, URANS, Purple: $\sigma=0.4$, "2D DES".

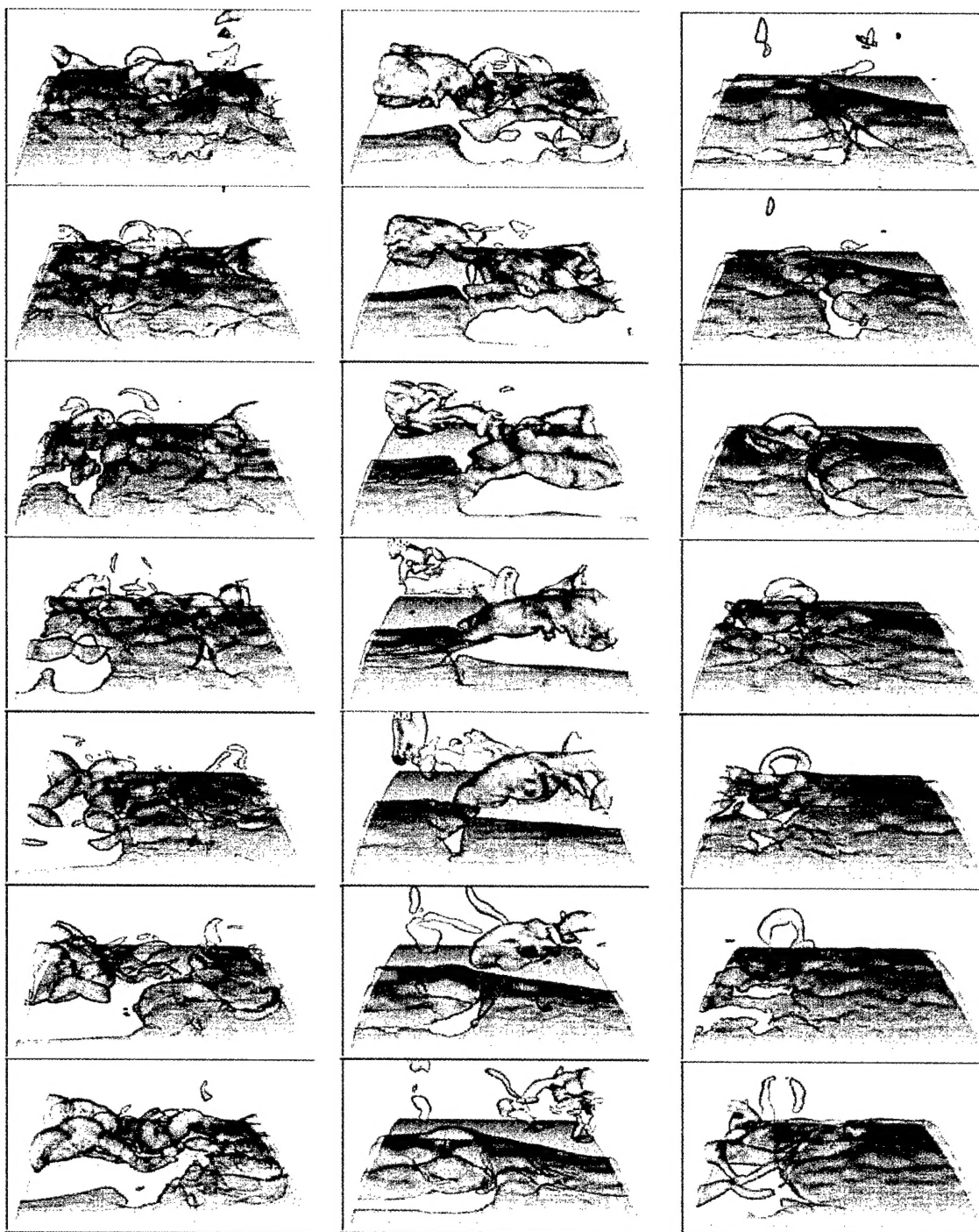


Figure 15: Composite of $\alpha_L=0.9$ isosurfaces for 21 timesteps between $t^*=15$ and 25^* for DES computation of $\sigma=0.8$ cavitating hydrofoil case.

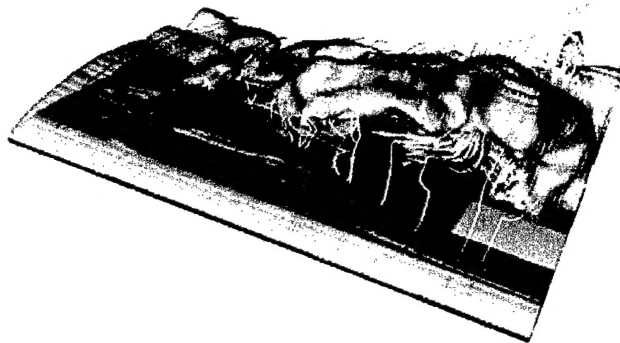


Figure 16: Isosurface of $\alpha_L=0.9$ with particle pathlines colored by static pressure at a given timestep for DES computation of $\sigma=0.8$ cavitating hydrofoil.

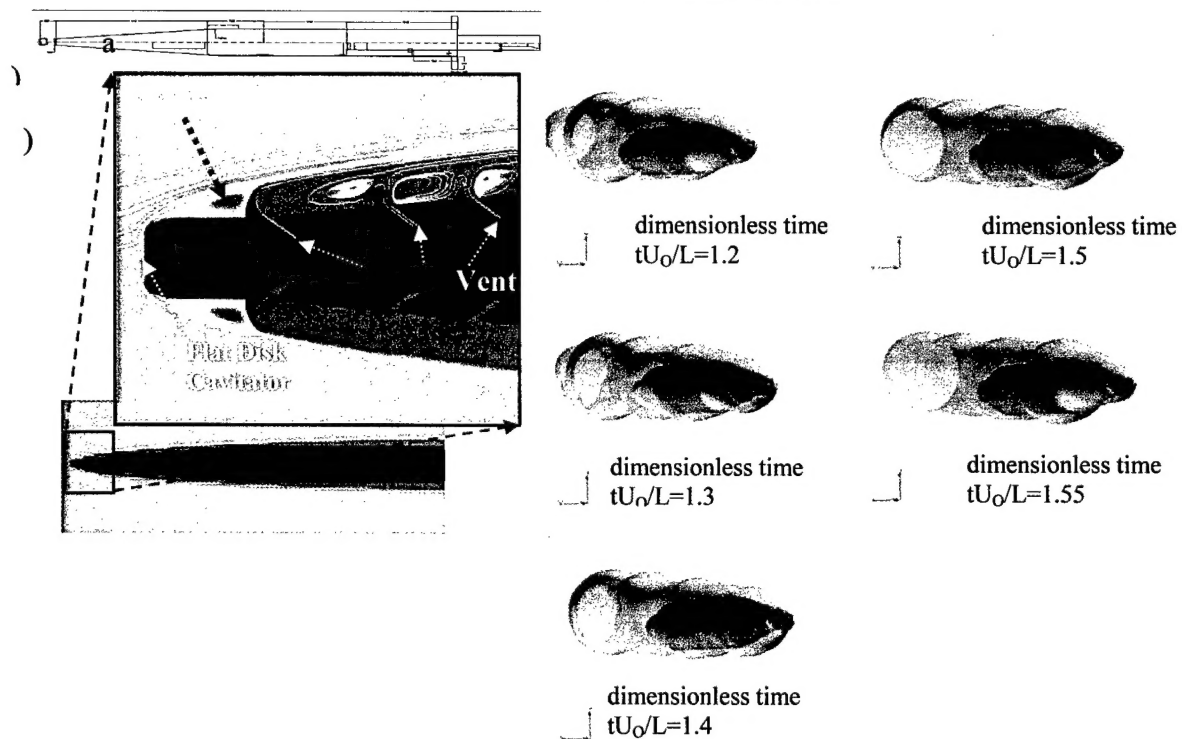


Figure 17: URANS-6DOF propelled supercavitating vehicle:

- Schematic (basis for notional model).
- Close-up of cavator/ventilator illustrating recirculatory behavior.
- Snapshots illustrated by translucent isosurface of constant volume fraction ($\alpha_L=0.5$) vehicle surface is colored by pressure level.

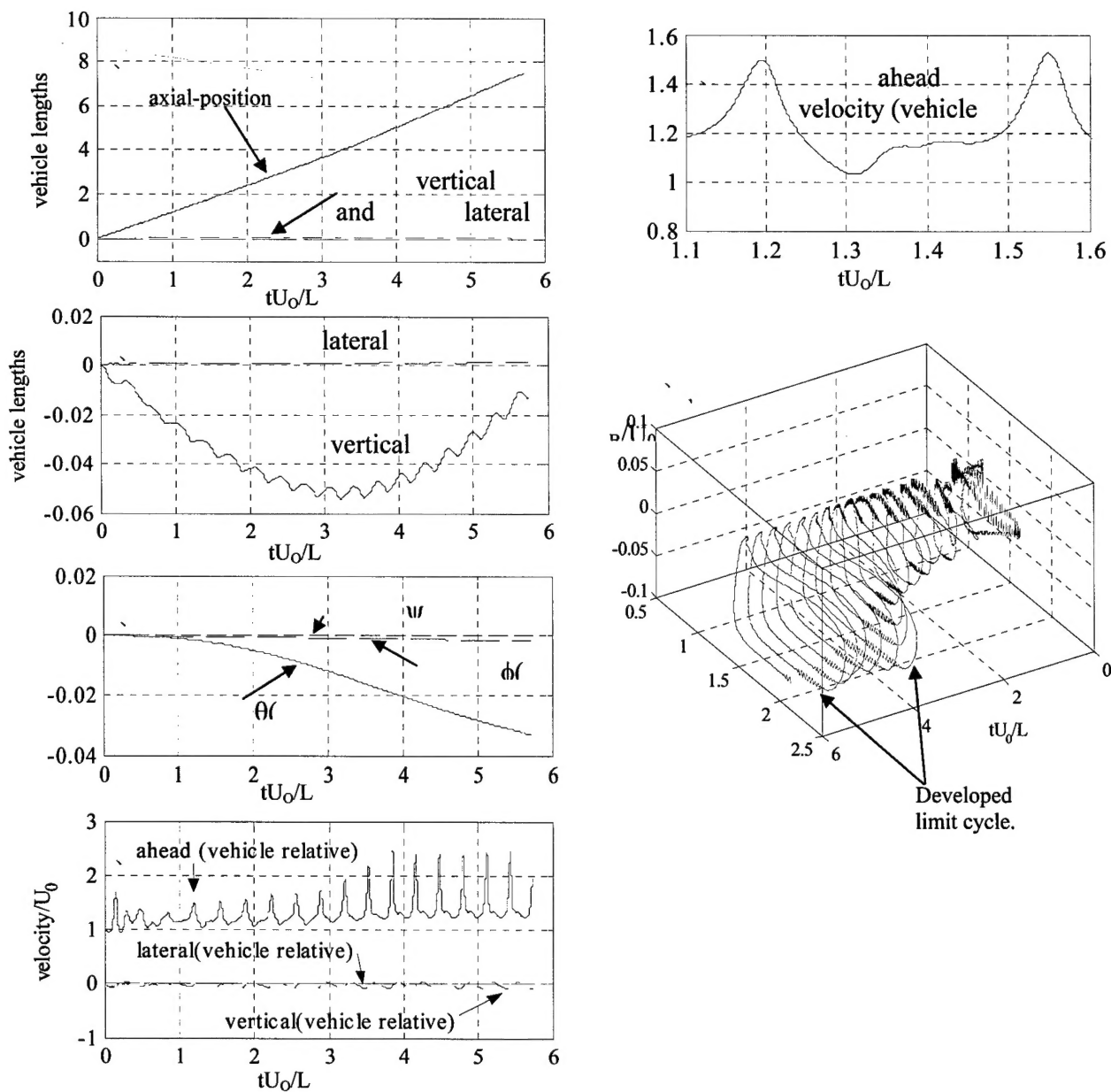


Figure 18: URANS-6DOF propelled supercavitating vehicle result: Time history plots. showing

- Absolute position.
- Lateral and vertical absolute positions.
- Rotation rates.
- Vehicle-relative velocities.
- Ahead velocity spanning a single period.
- Phase plot: ahead and vertical velocities over time.